

DETECTING ECCENTRIC SUPERMASSIVE BLACK HOLE BINARIES WITH PULSAR TIMING ARRAYS: RESOLVABLE SOURCE STRATEGIES

S. R. TAYLOR^{1*}, E. A. HUERTA², J. R. GAIR³, & S. T. MCWILLIAMS².

(Dated: June 26, 2015)
Draft version June 26, 2015

ABSTRACT

The couplings between supermassive black-hole binaries and their environments within galactic nuclei have been well studied as part of the search for solutions to the final parsec problem. The scattering of stars by the binary or the interaction with a circumbinary-disk may efficiently drive the system to sub-parsec separations, allowing the binary to enter a regime where the emission of gravitational-waves can drive it to merger within a Hubble time. However, these interactions can also affect the orbital parameters of the binary. In particular, they may drive an increase in binary eccentricity which survives until the system's gravitational-wave signal enters the pulsar-timing array band. Therefore, if we can measure the eccentricity from observed signals, we can potentially deduce some of the properties of the binary environment. To this end, we build on previous techniques to present a general Bayesian pipeline with which we can detect and estimate the parameters of an eccentric supermassive black-hole binary system with pulsar-timing arrays. Additionally, we generalize the pulsar-timing array \mathcal{F}_e -statistic to eccentric systems, and show that both this statistic and the Bayesian pipeline are robust when studying circular or arbitrarily eccentric systems. We explore how eccentricity influences the detection prospects of single gravitational-wave sources, as well as the detection penalty incurred by employing a circular waveform template to search for eccentric signals, and conclude by identifying important avenues for future study.

Subject headings: Gravitational waves – Methods: data analysis – Pulsars: general –

1. INTRODUCTION

The observation of extremely compact objects — black holes (BHs), neutron stars (NSs), and white dwarfs — and the development of a thorough theoretical understanding of their nature has been one of the triumphs of modern astrophysics (Chandrasekhar 1983; Misner et al. 1973; Thorne 1987), but there is still much that we do not understand about these exotic objects. The combination of electromagnetic observations with future detections of gravitational wave (GW) signals will provide key insights into the poorly understood astrophysical nature of compact objects and the role they play in some of the most energetic events in the Universe: gamma-ray bursts, active galactic nuclei, quasars, etc. (Hughes & Blandford 2003; Hughes 2009; Gebhardt et al. 2000; Soltan 1982; Peterson et al. 2004; Kormendy & Richstone 1995; Magorrian et al. 1998; Berger 2013; Berger et al. 2013; Janka et al. 1999; Lee & Ramirez-Ruiz 2007; Metzger & Berger 2012; Piran et al. 2013; Tanvir et al. 2013). Several large-scale collaborations are working to inaugurate the new field of GW astronomy by targeting a wide variety of potential GW sources. These range from the mergers of supermassive black hole binaries, which may be used by pulsar timing arrays to probe the innermost regions of merging galaxies, to the coalescence of NS binaries and stellar mass BHs, which encode important information about stellar evolution, galactic nuclei and globular clusters.

In this article, we will focus on a particular type of source that is being targeted by pulsar timing arrays (PTAs, Fos-

ter & Backer 1990). PTAs aim to observe GWs in the nanohertz frequency band via the accurate timing of millisecond pulsars. There are three major PTA collaborations — the European PTA, (EPTA, Kramer & Champion 2013), the North American Nanohertz Observatory for Gravitational-waves (NANOGrav, McLaughlin 2013) and the Parkes PTA (PPTA, Hobbs 2013) in Australia. These three collaborations also aim to cooperate as the International PTA (IPTA, Manchester & IPTA 2013).

The sources of interest in this work are individual binary systems of supermassive black holes (SMBHs) during their early inspiral evolution (Rajagopal & Romani 1995; Jaffe & Backer 2003; Wyithe & Loeb 2003; Sesana & Vecchio 2010; Sesana et al. 2009). Given the nature of these systems, i.e., large orbital separations and small local velocity of the binary components, we can take the compact objects as point-particles without internal dynamics and model the orbital evolution of the system using a post-Newtonian expansion (Peters & Mathews 1963; Barack & Cutler 2004; Sesana & Vecchio 2010). Furthermore, these events will be observed at large orbital separations, where the orbital evolution may be more strongly influenced by dynamical interactions with the astrophysical environment rather than GW emission. Hence, the circularizing influence of the latter may be lessened, allowing for quite large orbital eccentricities.

There are several mechanisms that could drive the eccentricity evolution of a SMBH binary (SMBHB). For instance, at sub-parsec scales a SMBHB formed by a galactic merger may be embedded in a dense stellar environment. As discussed in Sesana et al. (2008), if one assumes an isotropic stellar distribution, the interaction of a star and a SMBHB with semi major axis a can have two possible outcomes. Denoting the semi-major axis of the binary formed by the star and the SMBHB by a_* , encounters with stars with $a_* \lesssim a$ tend to circularize the orbit, whereas those with stars with $a_* \gtrsim a$

* email: Stephen.R.Taylor@jpl.nasa.gov

¹ Jet Propulsion Laboratory, California Institute of Technology, 4800 Oak Grove Drive, Pasadena, CA 91106, USA

² Department of Physics and Astronomy, West Virginia University, White Hall, Morgantown, WV 26506, USA

³ Institute of Astronomy, University of Cambridge, Madingley Rd., Cambridge, CB3 0HA, UK

tend to increase the eccentricity of the binary. In non-isotropic environments, co-rotation of the stellar distribution tends to circularize the binary. Counter-rotating stars tend to extract angular momentum from the SMBHB, causing the eccentricity to grow (Sesana et al. 2011). Several issues still remain to be explored regarding the evolution of SMBHBs at sub-parsec scales in dense stellar environments, but most models seem to favor a growth in orbital eccentricities before these systems enter the frequency band of PTAs (Sesana 2010; Roedig & Sesana 2012).

Aside from interactions with stars, the dynamical evolution of a SMBHB at sub-parsec orbital separations can also be influenced by the redistribution of energy and angular momentum between the binary and a self-gravitating disc. Consider a gaseous disc co-rotating with a binary, and define $\lambda \equiv R_t/a$, where R_t is the distance of the strongest torque on the binary as measured from the center of mass, and a is the semi-major axis of the binary. Detailed numerical simulations suggest that the evolution of the orbital eccentricity of a SMBHB embedded in a circumbinary disc is independent of the mass-ratio of the system, but depends sensitively on the location of the inner rim of the disc, λ , with respect to the binary's center of mass. For $2 < \lambda < 2.5$, it is expected that binaries will converge to a critical eccentricity value $0.55 < e_* < 0.79$. Binaries with initial eccentricities $e > e_*$ will undergo a steady decrease in eccentricity, whereas binaries with $e < e_*$ will experience the opposite behavior. The larger the separation between the rim of the disc and the center of mass of the binary, the longer the system will take to attain e_* (Roedig et al. 2011).

Taking into account these considerations, we recently introduced a theoretical framework to explore in detail the effect of eccentricity for source detection of potential PTA sources (Huerta et al. 2015). We now extend that analysis by introducing novel, accurate and efficient pipelines that shed light on the accuracy with which the astrophysical parameters of individually resolved eccentric SMBH binaries can be reconstructed. This analysis explores the impact of eccentricity both in terms of source detection and parameter estimation, and presents new statistics to facilitate the analysis. Our approach builds on previous Bayesian (Ellis 2013; Taylor et al. 2014) and frequentist (Babak & Sesana 2012; Ellis et al. 2012) statistics which have assumed circular gravitational waveform models, and unlike recent studies (Zhu et al. 2015) can recover all binary characteristics in addition to providing detection statistics.

This article is laid out as follows. In Section 2 we briefly review the orbital trajectories of eccentric binary systems, and how we can analytically solve for the orbital phase at a given time. This is followed in Sec. 3 by a description of the eccentric gravitational waveforms we use, and in Sec. 4 by our model of the perturbations these GWs induce in the times of arrival of radio signals from pulsars. The details of our analysis are provided in Sec. 5, followed by the results of Bayesian and frequentist signal recoveries from simulated datasets in Sec. 6. In Sec. 7, we discuss the likely impact of several assumptions that we have made which should be explored further in future studies. We finish with concluding remarks in Sec. 8. In the following we adopt units such that $G = c = 1$.

2. ECCENTRIC BINARY ORBITS

We briefly review the *Kepler problem* and present the general approach to analytically solve for the orbit of an eccentric binary, reiterating some of the notation and formalism of Yunes et al. (2009), and referring the reader to Goldstein

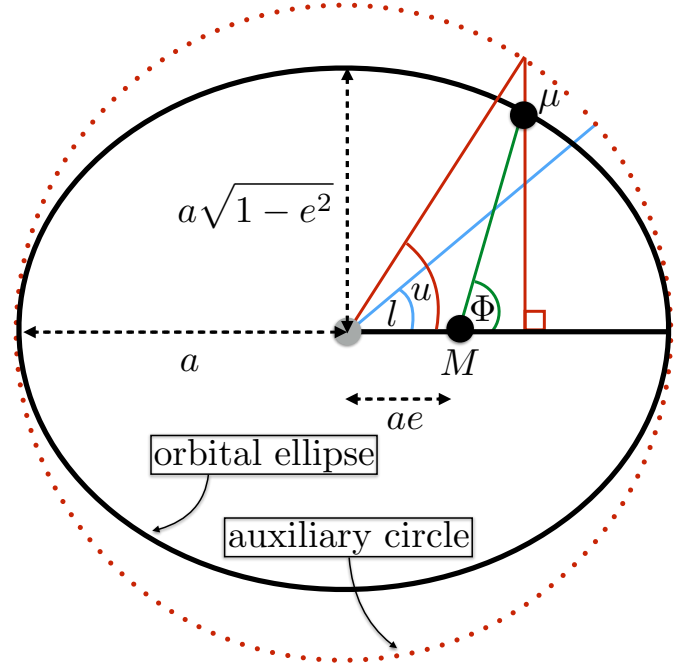


Figure 1. A diagram illustrating the relationship between the various angular elements in a binary system with orbital eccentricity e , reduced mass μ , and total mass M . The semi-major and semi-minor axes are a and $a\sqrt{1-e^2}$, respectively. If we measure the angles from the moment of periastris, then Φ is the true anomaly, l is the mean anomaly, and u is the eccentric anomaly. The auxiliary circle has a radius equal to the orbital semi-major axis.

(1950) for a more complete discussion of the Kepler problem.

We consider a binary system with component masses m_1 and m_2 , total mass M , and a reduced mass $\mu = m_1 m_2 / (m_1 + m_2)$. The separation vector joining the components is defined in terms of the component position vectors by $\vec{r} = \vec{r}_1 - \vec{r}_2$, such that $\vec{r}_1 = m_2 \vec{r} / M$ and $\vec{r}_2 = -m_1 \vec{r} / M$. Using $(r = |\vec{r}|, \Phi)$ to denote plane polar coordinates for the position of one member of the binary with respect to the other, the Newtonian Keplerian orbital trajectories of two point particles in an eccentric binary system are described by

$$r = a(1 - e \cos u), \quad (1)$$

$$\omega(t - t_0) = l = u - e \sin u, \quad (2)$$

$$\Phi - \Phi_0 = v \equiv 2 \arctan \left[\left(\frac{1+e}{1-e} \right)^{1/2} \tan \frac{u}{2} \right], \quad (3)$$

where a is the semi-major axis of the orbit; and $0 \leq e < 1$ is the eccentricity (of a bound orbit). The *eccentric anomaly*, u , is an auxiliary variable with which to parametrize the radial and phase coordinates. Given the average angular frequency (or *mean motion*; $\omega = 2\pi/T$, where T is the orbital period) and eccentricity of the orbit, we can solve the transcendental Eq. (2) for u at a given time t , where $l = 2\pi(t - t_0)/T$ is denoted as the *mean anomaly*. The eccentric anomaly can then be plugged into Eqs. (1) and (3) to give the separation and orbital phase (or *true anomaly*; $\Phi - \Phi_0$) at any point along the orbital trajectory. If we assume that time and phase are measured from the moment of periastris, then the constants of integration t_0 and Φ_0 can be set to zero. All of these angular quantities are shown diagrammatically for an example orbital ellipse in Fig. 1.

The flux of energy and angular-momentum carried away from the system by GWs depend on the eccentricity and the Keplerian mean orbital frequency, F . Once the binary evolution is driven solely by GW emission, these co-evolve as (Peters 1964)

$$\frac{F(e)}{F(e_0)} = \left(\frac{\sigma(e_0)}{\sigma(e)} \right)^{3/2}, \quad (4)$$

where

$$\sigma(e) = \frac{e^{12/19}}{1-e^2} \left[1 + \frac{121}{304} e^2 \right]^{870/2299}, \quad (5)$$

and e_0 is defined as the eccentricity of the system at some earlier reference epoch of the binary evolution.

The frequency F can be regarded as the *instantaneous mean orbital frequency*. For GW-dominated orbital evolution, it co-evolves with the eccentricity according to the coupled differential equations (Peters 1964)

$$\begin{aligned} \frac{dF}{dt} &= \frac{48}{5\pi\mathcal{M}^2} (2\pi\mathcal{M}F)^{11/3} \frac{1 + \frac{73}{24}e^2 + \frac{37}{96}e^4}{(1-e^2)^{7/2}}, \\ \frac{de}{dt} &= -\frac{304}{15\mathcal{M}} (2\pi\mathcal{M}F)^{8/3} e \frac{1 + \frac{121}{304}e^2}{(1-e^2)^{5/2}}, \end{aligned} \quad (6)$$

where $\mathcal{M} = (m_1 m_2)^{3/5} / (m_1 + m_2)^{1/5}$ is the binary chirp mass.

Gravitational waveform templates describing the emission from inspiraling binary systems depend on trigonometric functions of the orbital phase. For circular systems the relationship between orbital frequency, time, and phase is simple: we have $\Phi = 2\pi \int F(t) dt$, where $F(t)$ is the Keplerian orbital-frequency (half of the dominant quadrupole GW frequency) which evolves according to Eq. (6) with $e = 0$. However the situation is rather more complicated for eccentric systems. The phase is related via an arctangent to the eccentric anomaly, which is then related to the mean anomaly (and thus the mean angular frequency $\omega = 2\pi F$) via a transcendental equation. The so-called *Kepler problem* refers to the historical difficulty in finding solutions to the transcendental equation in Eq. (2) and thus being able to express the orbital phase in terms of the mean anomaly. We do so using the well known Fourier analysis of the Kepler problem. For full details of the calculation see Watson (1995), or Appendix A (where it is given for completeness). Using elementary properties of elliptic curves and Bessel functions, the results are

$$\cos \Phi = -e + \frac{2}{e} (1-e^2) \sum_{n=1}^{\infty} J_n(ne) \cos(nl), \quad (7)$$

$$\sin \Phi = (1-e^2)^{1/2} \sum_{n=1}^{\infty} [J_{n-1}(ne) - J_{n+1}(ne)] \sin(nl). \quad (8)$$

With these trigonometric functions of the orbital phase, we can now construct gravitational waveforms for eccentric inspiraling binary systems in terms of the mean orbital frequency. Equations (7) and (8) can be immediately used to construct these waveforms. However, by setting a required tolerance on the accuracy of $\sin \Phi$ and $\cos \Phi$ for a given eccentricity, we can truncate the infinite summations (Pierro et al. 2001; Yunes et al. 2009) to accelerate calculations. We investigate the minimum number of terms required for the Fourier series expansion of $\cos \Phi$ in Eq. (7) to maintain accuracy with the exact numerical solution of Eqs. (1)-(3), by demanding

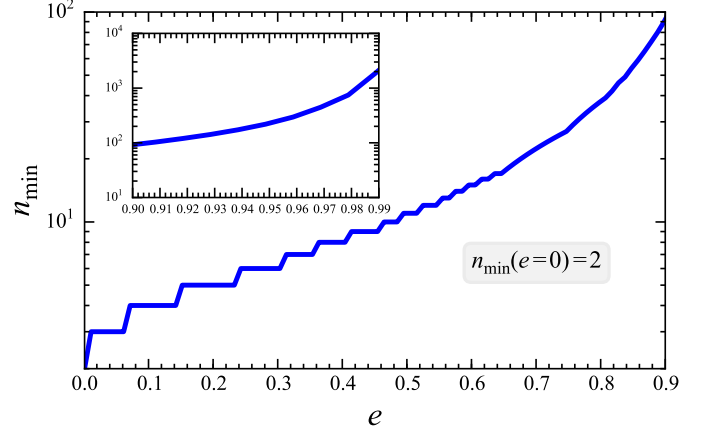


Figure 2. The minimum number of harmonics required for the Fourier solution of $\cos \Phi$ as a function of l (mean anomaly) to maintain accuracy with the numerical solution. We demand that the overlap of the Fourier solution and numerical solution, as determined by the normalized scalar product of the two solution vectors, is $> 99.999\%$ over 2π of mean anomaly.

that the error in the two solutions (determined by the normalized scalar product between the two solution vectors) is less than 0.001% over 2π of mean-anomaly. The results are shown in Fig. 2, where we see that $\lesssim 100$ terms in the summation are necessary to maintain accuracy up to $e = 0.9$, however the required number of terms dramatically increases beyond 0.9, exceeding 10^3 at $e = 0.99$. Although systems with high residual eccentricity (> 0.9) in the sub-parsec GW inspiral regime may exist, they are by no means expected to be common. Hence, we restrict our attention to systems with eccentricity below 0.9, in which regime highly accurate waveforms require the inclusion of fewer than 100 Fourier terms.

3. ECCENTRIC TIME-DOMAIN WAVEFORMS

In the transverse-traceless gauge the GW-tensor can be written as a linear superposition of “plus” and “cross” polarization modes, with associated polarization-amplitudes, $h_{\{+, \times\}}$, and basis-tensors, $e_{ab}^{\{+, \times\}}(\hat{\Omega})$, such that

$$h_{ab}(t, \hat{\Omega}) = h_+(t) e_{ab}^+(\hat{\Omega}) + h_\times(t) e_{ab}^\times(\hat{\Omega}), \quad (9)$$

where $\hat{\Omega}$ is defined as the direction of GW propagation.

We employ the Peters-Mathews waveforms (Peters & Mathews 1963) given by Barack & Cutler (2004), which make use of the Fourier analysis of the Kepler problem to give the following analytic expressions for h_+ and h_\times :

$$\begin{aligned} h_+(t) &= \sum_n -(1 + \cos^2 \iota) [a_n \cos(2\gamma) - b_n \sin(2\gamma)] \\ &\quad + (1 - \cos^2 \iota) c_n, \\ h_\times(t) &= \sum_n 2 \cos \iota [b_n \cos(2\gamma) + a_n \sin(2\gamma)], \end{aligned} \quad (10)$$

where

$$\begin{aligned} a_n &= -n\zeta\omega^{2/3} [J_{n-2}(ne) - 2eJ_{n-1}(ne) + (2/n)J_n(ne) \\ &\quad + 2eJ_{n+1}(ne) - J_{n+2}(ne)] \cos[nl(t)], \\ b_n &= -n\zeta\omega^{2/3} \sqrt{1-e^2} [J_{n-2}(ne) - 2J_n(ne) + J_{n+2}(ne)] \sin[nl(t)], \\ c_n &= 2\zeta\omega^{2/3} J_n(ne) \cos[nl(t)]. \end{aligned} \quad (11)$$

The amplitude parameter is defined as $\zeta = \mathcal{M}^{5/3}/D_L$, where D_L is the luminosity distance of the binary, and $\omega = 2\pi F$. The

mean anomaly is $l(t) = l_0 + 2\pi \int_{t_0}^t F(t') dt'$ [where l_0 is the mean anomaly at t_0]; γ is an azimuthal angle measuring the direction of pericenter with respect to $\hat{x} \equiv (\hat{\Omega} + \hat{L} \cos \iota) / \sqrt{1 - \cos^2 \iota}$; and ι is the binary orbital inclination angle, defined by $\cos \iota = -\hat{L} \cdot \hat{\Omega}$. In the following, F and \mathcal{M} refer to the observed redshifted values, such that $F_r = F(1+z)$ and $\mathcal{M}_r = \mathcal{M}/(1+z)$, where F_r and \mathcal{M}_r are rest frame values, and z is the cosmological redshift of the binary.

An important feature to emphasize here is that eccentric binaries do not radiate monochromatic GWs, but rather emit a spectrum of frequencies which are harmonics of the mean orbital frequency. Given that $J_0(0) = 1$ and $J_{n>0}(0) = 0$, it is immediately obvious from Eqs. (10) and (11) that $e = 0$ waveforms will only include the $n = 2$ harmonic of the binary's mean orbital frequency. This is the usual result that the GW frequency of emission from circular binaries is twice the orbital frequency.

To construct the polarization basis tensors, we define a right-handed basis triad in terms of $\{\hat{n}, \hat{p}, \hat{q}\}$, where $\hat{n} = -\hat{\Omega}$, $\hat{p} = (\hat{n} \times \hat{L}) / |\hat{n} \times \hat{L}|$ and $\hat{q} = \hat{p} \times \hat{n}$. The vectors comprising the basis triad are explicitly

$$\hat{n} = (\sin \theta \cos \phi, \sin \theta \sin \phi, \cos \theta), \quad (12)$$

$$\hat{p} = (\cos \psi \cos \theta \cos \phi - \sin \psi \sin \phi, \cos \psi \cos \theta \sin \phi + \sin \psi \cos \phi, -\cos \psi \sin \theta), \quad (13)$$

$$\hat{q} = (\sin \psi \cos \theta \cos \phi + \cos \psi \sin \phi, \sin \psi \cos \theta \sin \phi - \cos \psi \cos \phi, -\sin \psi \sin \theta), \quad (14)$$

where $(\theta, \phi) = (\pi/2 - \text{DEC}, \text{RA})$ denotes the sky-location of the binary in spherical polar coordinates, and ψ corresponds to the angle between \hat{p} and the line of constant azimuth when the orbit is viewed from the origin of our coordinate system. These angles are shown diagrammatically in Fig. 3. The vectors \hat{p} and \hat{q} lie in the transverse plane to the direction of GW propagation, and are used to construct basis tensors as follows:

$$e_{ab}^+ = \hat{p}_a \hat{p}_b - \hat{q}_a \hat{q}_b, \quad (15)$$

$$e_{ab}^\times = \hat{p}_a \hat{q}_b + \hat{q}_a \hat{p}_b. \quad (16)$$

4. PULSAR TIMING RESIDUALS INDUCED BY AN ECCENTRIC BINARY

As a GW transits across the line of sight between a pulsar and the Earth, it creates a perturbation in the space-time metric which causes a change in the proper separation between the Earth and the pulsar. This in turn leads to a shift in the perceived pulsar rotational frequency. The fractional frequency shift of a signal from a pulsar in the direction of unit vector \hat{u} , induced by the passage of a single GW propagating in the direction of $\hat{\Omega}$ is (Anholm et al. 2009; Book & Flanagan 2011)

$$z(t, \Omega) = \frac{1}{2} \frac{\hat{u}^a \hat{u}^b}{1 + \hat{\Omega} \cdot \hat{u}} \Delta h_{ab}(t, \Omega), \quad (17)$$

where $\Delta h_{ab} \equiv h_{ab}(t_e, \hat{\Omega}) - h_{ab}(t_p, \hat{\Omega})$ is the difference in the metric perturbation evaluated at time t_e when the GW passed the solar system barycenter (SSB) and time t_p when the GW passed the pulsar. From simple geometrical arguments, we can write $t_p = t_e - L(1 + \hat{\Omega} \cdot \hat{u})$, where L is the distance to the pulsar. The integrated effect of this GW-induced *redshift* over the total observing time of the pulsar leads to an offset be-

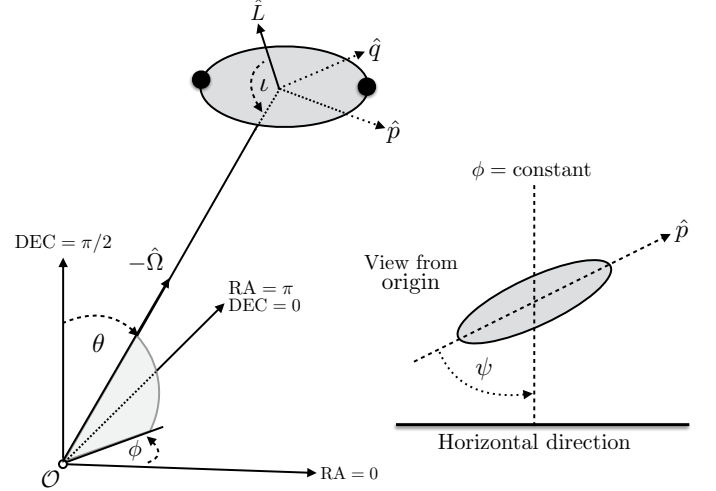


Figure 3. A diagram illustrating the geometry of an eccentric SMBH binary with respect to the angles of our coordinate system. The unit vector pointing to the binary is $\hat{n} = -\hat{\Omega}$, with spherical-polar coordinates $\{\theta = \pi/2 - \text{DEC}, \phi = \text{RA}\}$. The binary orbital inclination angle is defined by $\cos \iota = \hat{L} \cdot \hat{n}$, where \hat{L} is a unit vector pointing along the binary's orbital angular momentum. The GW polarization basis tensors are defined in the plane transverse to the direction of propagation, in terms of the unit vectors $\hat{p} = (\hat{n} \times \hat{L}) / |\hat{n} \times \hat{L}|$ and $\hat{q} = \hat{p} \times \hat{n}$, where $\{\hat{n}, \hat{p}, \hat{q}\}$ define a right-handed basis triad. The vector \hat{p} lies along the major axis of the projected ellipse as seen from the origin of the coordinate system. The GW polarization angle ψ is defined as the angle between \hat{p} and the line of constant azimuth. This diagram is a modified version of Fig. 1 in Apostolatos et al. (1994).

tween the expected and the observed pulse TOA:

$$s(t) = \int_0^t z(t') dt'. \quad (18)$$

The expected pulse TOA is computed from a deterministic timing model which characterizes a pulsar's astrometric and spin properties. This model is refined over many observations to give an accurate prediction of the pulse arrival times. The difference between the measured TOAs and those predicted by the best-fit deterministic timing-model are the *timing residuals*. In addition to any GW signals, these residuals encode the influence of noise processes and all unmodelled phenomena which affect pulsar TOAs. The pulsar timing residuals induced by a single GW source can be written as

$$s(t, \hat{\Omega}) = F^+(\hat{\Omega}) \Delta s_+(t) + F^\times(\hat{\Omega}) \Delta s_\times(t), \quad (19)$$

where $A = \{+, \times\}$, $\Delta s_A(t) = s_A(t_e) - s_A(t_p)$, with $s_A(t) = \int_0^t h_A(t') dt'$, and $F^A(\hat{\Omega})$ are *antenna pattern response functions* encoding the geometrical sensitivity of a particular pulsar to a propagating GW, defined as

$$F^A(\hat{\Omega}) \equiv \frac{1}{2} \frac{\hat{u}^a \hat{u}^b}{1 + \hat{\Omega} \cdot \hat{u}} e_{ab}^A(\hat{\Omega}), \quad (20)$$

and corresponding to the contraction of the pulsar-timing impulse response function with the GW polarization basis tensors.

The form of $s_A(t)$ can be computed analytically by assuming that the binary's mean orbital frequency and eccentricity remain constant over the total timespan of our observations of a given pulsar. More specifically, we must assume no binary evolution over the Earth term timing baseline, $[t_e, t_e + T]$, and also the corresponding timing baseline of the pulsar term, $[t_e - L(1 + \hat{\Omega} \cdot \hat{u}), t_e + T - L(1 + \hat{\Omega} \cdot \hat{u})]$, where T is $\mathcal{O}(10 \text{ years})$. Therefore, time only appears in the definition of the mean anomaly as a linear parameter, such that $l(t) =$

$l_0 + 2\pi \int_{t_0}^t F(t') dt' = l_0 + 2\pi F(t - t_0)$, which allows $\cos[nl(t)]$ and $\sin[nl(t)]$ in Eq. (11) to be trivially integrated to give the plus/cross residuals:

$$\begin{aligned} s_+(t) &= \sum_n -(1 + \cos^2 \iota) [a_n \cos(2\gamma) - b_n \sin(2\gamma)] \\ &\quad + (1 - \cos^2 \iota) c_n, \\ s_\times(t) &= \sum_n 2 \cos \iota [b_n \cos(2\gamma) + a_n \sin(2\gamma)], \end{aligned} \quad (21)$$

where

$$\begin{aligned} a_n &= -\zeta \omega^{-1/3} [J_{n-2}(ne) - 2eJ_{n-1}(ne) + (2/n)J_n(ne) \\ &\quad + 2eJ_{n+1}(ne) - J_{n+2}(ne)] \sin[nl(t)] \\ &= \zeta \omega^{-1/3} x_{a_n} \sin[nl(t)], \\ b_n &= \zeta \omega^{-1/3} \sqrt{1-e^2} [J_{n-2}(ne) - 2J_n(ne) + J_{n+2}(ne)] \cos[nl(t)] \\ &= \zeta \omega^{-1/3} x_{b_n} \cos[nl(t)], \\ c_n &= (2/n) \zeta \omega^{-1/3} J_n(ne) \sin[nl(t)] \\ &= \zeta \omega^{-1/3} x_{c_n} \sin[nl(t)], \end{aligned} \quad (22)$$

and the quantities $\{x_{a_n}, x_{b_n}, x_{c_n}\}$ are defined for later convenience.

We can now analyze the harmonic content of the variance of the residuals from both plus and cross polarizations, which is computed over one period of binary elliptical motion ($l = \{0, 2\pi\}$) and over $\cos \iota, \gamma$. Clearly averaging over a single (or any non-zero integer) period of orbital motion is only an approximation, since our pulsar-timing observations are highly unlikely to span an integer number of orbital periods or GW cycles. Nevertheless we carry out this calculation since it illuminates certain features of the harmonic content of the GW signal from eccentric SMBH binaries. We employ the following relations when averaging over the mean anomaly:

$$\int_0^{2\pi} dl \sin(nl) \cos(n'l) = 0, \quad \forall n, n', \quad (23)$$

$$\int_0^{2\pi} dl \sin(nl) \sin(n'l) = \begin{cases} 0, & \text{if } n \neq n', \\ \pi, & \text{if } n = n', \end{cases} \quad (24)$$

where $n, n' \geq 1$, and the last equation is also true for cosine functions. Given that the induced residuals are zero-mean over integers of the binary orbital period, the resulting variance of the residuals is

$$\langle s_A^2 \rangle = \zeta^2 \omega^{-2/3} \sum_n \langle s_A^2 \rangle_n, \quad (25)$$

where

$$\begin{aligned} \langle s_+^2 \rangle_n &= \frac{7}{15} (x_{a_n}^2 + x_{b_n}^2) + \frac{4}{15} x_{c_n}^2, \\ \langle s_\times^2 \rangle_n &= \frac{1}{3} (x_{a_n}^2 + x_{b_n}^2). \end{aligned} \quad (26)$$

The value of $\langle s_+^2 \rangle_n$ for several binary eccentricities is shown in the left panel of Fig. 4. At each eccentricity, the contribution of each harmonic to the variance of the residuals is normalized with respect to the largest contribution. In the right panel of Fig. 4 we show the fraction of the total variance of the plus-component timing residuals contributed by the dominant harmonic, which switches from $n=2$ in the $0 \leq e \lesssim 0.4$ range to $n=1$ beyond $e \sim 0.4$.

For the remainder of this paper we will present results from investigations with the Earth term of the GW-induced timing residuals. The signal model in Eq. (21) is general, and can be used to compute both Earth and pulsar terms, modulo the assumption of binary non-evolution over typical pulsar timing baselines. However, including the pulsar term requires either precision knowledge of the individual pulsar distances, or the distances to be searched or marginalized over (Ellis 2013; Taylor et al. 2014). This search over distance brings its own challenges since the likelihood is highly sensitive to small changes in the sampled distance around the true value, and can lead to inefficient sampling. We defer considerations of the pulsar term to future work, but will briefly consider its influence in Sec. 7. Furthermore, for the most extreme combinations of binary mass, eccentricity, and orbital frequency, the system may exhibit frequency chirping and orbital circularization during typical pulsar-timing observation timespans, rendering the assumption of non-evolution invalid. We explore these issues in Sec. 7 amid suggestions for future directions.

Related to these two issues are the fact that in general we would also need to consider evolution of the direction of pericenter, $\dot{\gamma}$, and orbital plane precession from spin-orbit coupling. Evolution of the direction of pericenter can occur even for circular binary systems composed of non-spinning black holes, leading to phase shifts and recovery bias in the orbital frequency if not considered. However, as discussed in Sesana & Vecchio (2010), these factors can be safely ignored over typical PTA observation timespans. In Fig. 5 we show exclusion regions in $\{M = (m_1 + m_2), F, e\}$ parameter space, where pericenter direction evolution leads to a bias in the orbital frequency which is greater than the typical PTA frequency resolution of $1/T$ for a 10 year observation timespan (Sesana & Vecchio 2010). The excluded regions correspond to systems with very high total mass and eccentricity, and orbital frequencies beyond the region of peak PTA sensitivity. Hence, we ignore this effect here and consider only $\{F, e\}$ evolution in Sec. 7, but information from these additional effects may allow the individual binary component masses, and possibly their spin, to be constrained (Mingarelli et al. 2012). Additionally, these effects are likely to be highly important when tracing the binary evolution back by thousands of years to the pulsar term.

5. DATA ANALYSIS OF TIMING RESIDUALS

5.1. Bayesian inference

Bayesian inference provides a robust framework within which we can map our belief in the measurement of model parameters to probability distributions. Bayes' theorem states that the *posterior* probability density function (PDF), $p(\vec{\mu}|D, \mathcal{H})$, of the parameters $\vec{\mu}$ within a model \mathcal{H} , and given data D is

$$p(\vec{\mu}|D, \mathcal{H}) = \frac{p(D|\vec{\mu}, \mathcal{H})p(\vec{\mu}|\mathcal{H})}{p(D|\mathcal{H})}, \quad (27)$$

where,

$$\begin{aligned} p(D|\vec{\mu}, \mathcal{H}) &\equiv \mathcal{L}(\vec{\mu}|D) = \text{likelihood of parameters,} \\ p(\vec{\mu}|\mathcal{H}) &\equiv \pi(\vec{\mu}) = \text{prior PDF of parameters,} \\ p(D|\mathcal{H}) &\equiv \mathcal{Z} = \text{Bayesian evidence.} \end{aligned} \quad (28)$$

The function $\mathcal{L}(\vec{\mu})$ denotes the likelihood of model parameters, $\vec{\mu}$, given observed data, D , and is equated to the probability of measuring this data given the model parameters. The posterior probability, $p(\vec{\mu}|D, \mathcal{H})$ is a measure of our belief in

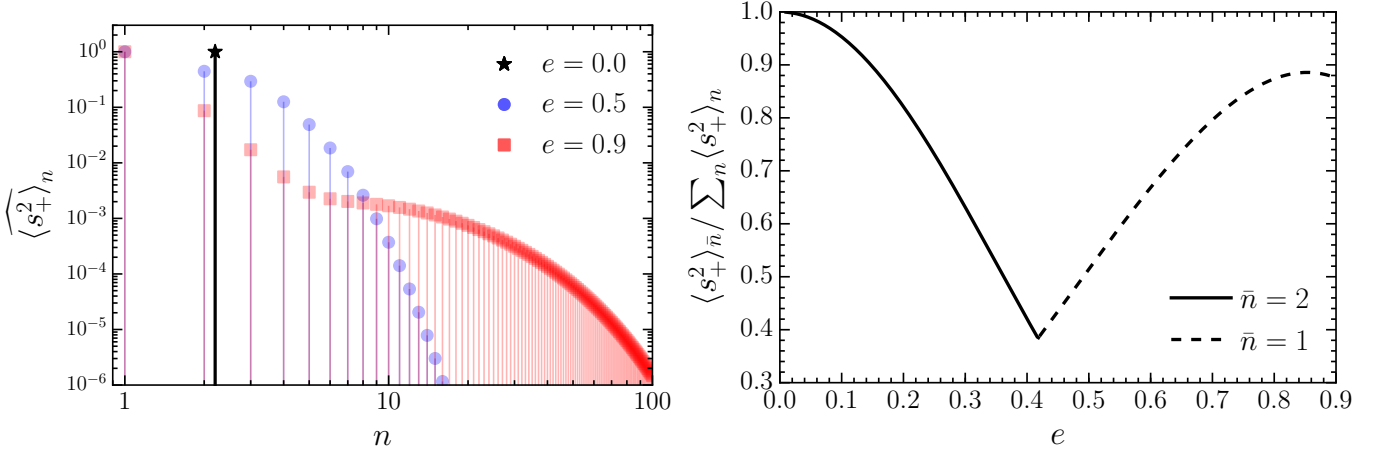


Figure 4. (Left): The contribution of each harmonic of the orbital frequency to the variance of the plus-component timing residuals. At each eccentricity we normalize the contributions from each harmonic with respect to the maximum contribution. The only contribution for circular binaries is from the second harmonic (black star and line, slightly offset from $n = 2$ for ease of viewing). At higher eccentricities ($e = 0.5, 0.9$) the contribution is spread into a spectrum of higher harmonics, but is dominated by the fundamental harmonic. (Right): The fraction of the total variance contributed by the dominant harmonic, \bar{n} , as a function of eccentricity. As in the left panel, n labels the harmonic of the binary mean orbital frequency. In the range $0 \leq e \lesssim 0.4$ the second harmonic dominates, whilst beyond $e \sim 0.4$ the fundamental harmonic dominates the variance of the induced timing residuals.

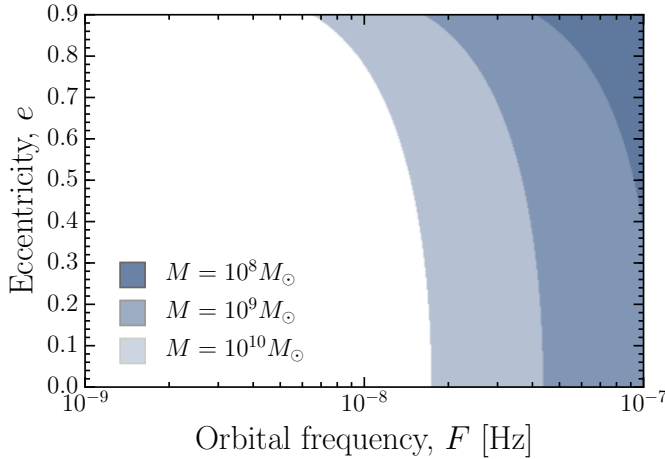


Figure 5. Exclusion regions in binary eccentricity and orbital frequency as a function of binary total mass, corresponding to parameter combinations where unmodelled evolution of binary pericenter direction causes a bias in orbital frequency recovery which could be resolved by 10 years of PTA observations, $\Delta f = 1/T = 3.2$ nHz.

the inference of a set of model parameters $\vec{\mu}$ from a single experiment, and will not necessarily coincide with the likelihood if we have non-trivial prior constraints.

We model the noise in our searches as random Gaussian processes, such that the likelihood function for signal parameters is

$$\mathcal{L}(\vec{\mu}) = \frac{\exp \left[-\frac{1}{2} (\delta \mathbf{t} - \mathbf{s}(\vec{\mu})) \mathbf{G} (\mathbf{G}^T \mathbf{C} \mathbf{G})^{-1} \mathbf{G}^T (\delta \mathbf{t} - \mathbf{s}(\vec{\mu})) \right]}{\sqrt{\det(2\pi \mathbf{G}^T \mathbf{C} \mathbf{G})}} \quad (29)$$

where $\delta \mathbf{t}$ and \mathbf{s} are the concatenated timing residuals (computed from the data) and model residuals (a function of signal parameters, $\vec{\mu}$) from all pulsars:

$$\delta \mathbf{t} = \begin{bmatrix} \delta t_1 \\ \delta t_2 \\ \vdots \\ \delta t_{N_p} \end{bmatrix}, \quad \mathbf{s} = \begin{bmatrix} \mathbf{s}_1 \\ \mathbf{s}_2 \\ \vdots \\ \mathbf{s}_{N_p} \end{bmatrix}, \quad (30)$$

and \mathbf{G} is a block-diagonal matrix (with a block for each pulsar) which projects our quantities into a space which is orthogonal to each pulsar's timing model. This matrix arises from an analytic marginalization over the modeled pulsar astrometric/spin properties with uniform priors (van Haasteren & Levin 2013). The matrix \mathbf{C} models the covariance in the TOAs arising from stochastic processes, which could include a GW stochastic background.

The Bayesian evidence, \mathcal{Z} , is the probability of the observed data given the model \mathcal{H}

$$\mathcal{Z} = \int \mathcal{L}(\vec{\mu}) \pi(\vec{\mu}) d\vec{\mu}. \quad (31)$$

For posterior inference within a model, \mathcal{Z} plays the role of a normalization constant and can be ignored. However, if we want to perform model selection then this evidence value becomes key. In Bayesian model comparison we compute the posterior odds ratio:

$$\frac{p(\mathcal{H}_2|D)}{p(\mathcal{H}_1|D)} = \frac{p(D|\mathcal{H}_2)p(\mathcal{H}_2)}{p(D|\mathcal{H}_1)p(\mathcal{H}_1)} = \frac{\mathcal{Z}_2 \times p(\mathcal{H}_2)}{\mathcal{Z}_1 \times p(\mathcal{H}_1)}. \quad (32)$$

where $\mathcal{Z}_2/\mathcal{Z}_1$ is the Bayes factor, and $p(\mathcal{H}_2)/p(\mathcal{H}_1)$ is the prior probability ratio for the two competing models. Since the evidence is the average of the likelihood over the prior volume, it automatically incorporates Occam's razor: a simpler theory with a compact parameter space will have larger evidence than a more complicated one, unless the latter is significantly better at explaining the data. Hypothesis \mathcal{H}_2 is chosen if the posterior odds ratio is sufficiently large.

5.2. Signal to noise ratio (SNR)

The signal to noise ratio (SNR, ρ) provided by a particular GW signal template, \mathbf{s} , in a matched-filtering search of measured timing residuals, $\delta \mathbf{t}$, is (Finn 2001)

$$\rho = \frac{(\delta \mathbf{t} | \mathbf{s})}{\sqrt{(\mathbf{s} | \mathbf{s})}}, \quad (33)$$

where the vectors are concatenated over all pulsars in an array, and the inner product is defined as $(x|y) = x^T \mathbf{G} (\mathbf{G}^T \mathbf{C} \mathbf{G})^{-1} \mathbf{G}^T y$,

with \mathbf{G} being the previously defined timing-model marginalization matrix. The optimal SNR is obtained by maximizing the noise-averaged SNR over signal templates, to give

$$\rho_{\text{opt}} = \sqrt{(\mathbf{s}|\mathbf{s})}, \quad (34)$$

where \mathbf{s} is now the true signal in the data. This quantity provides a measure of the detectability of a signal constructed from certain binary parameters in pulsars with certain noise properties. We will make use of both the optimal SNR and matched-filtering SNR in the following analyses.

5.3. Markov chain Monte Carlo analysis

Markov Chain Monte Carlo (MCMC) techniques provide an efficient way to explore a model's parameter space, and thereby reconstruct the joint posterior probability distribution of model parameters in a Bayesian analysis. An initial point in parameter space, \vec{x}_0 , is drawn from the *prior* probability distribution of parameters, which is followed at each subsequent iteration, i , by drawing a new point, \vec{y} , from a *proposal distribution*, $q(\vec{y}|\vec{x})$, and the evaluation of the Metropolis-Hastings ratio,

$$R = \frac{\pi(\vec{y})\mathcal{L}(\vec{y})q(\vec{x}_i|\vec{y})}{\pi(\vec{x}_i)\mathcal{L}(\vec{x}_i)q(\vec{y}|\vec{x}_i)}. \quad (35)$$

A random sample, u , is drawn from a uniform distribution, $u \in U[0, 1]$, and if $u < R$ the move to the new point is accepted and we set $\vec{x}_{i+1} = \vec{y}$. If $u > R$, the move is rejected and we set $\vec{x}_{i+1} = \vec{x}_i$. If the sampling procedure is ergodic then the distribution of independent samples will converge to the target posterior distribution. There are many sophisticated techniques to ensure efficient mixing of the chain of samples and to minimize the chain autocorrelation length.⁵ The MCMC samples can be used to carry out integrals of arbitrary functions, $f(\vec{x})$, over the posterior

$$\int f(\vec{x})p(\vec{x}|D, \mathcal{H})d\vec{x} \approx \frac{1}{N_{\text{samples}}} \sum_{i=1}^{N_{\text{samples}}} f(\vec{x}_i). \quad (36)$$

The marginalized posterior probability distribution for a subset of parameters follows by binning the chain samples in that subset, e.g. a 1D posterior PDF is determined from the histogram of samples in the parameter of interest.

5.4. Simulated datasets

For our proof-of-principle study of an eccentric single-source pipeline, we consider the array of 36 pulsars from the IPTA mock data challenge.⁶ They are timed to 100 ns precision over a timing baseline of 10 years, with observations carried out every 4 weeks. This array is obviously idealized, however the generalization to more realistic observing schedules and pulsar noise properties will not require modifications to our pipeline since it is constructed in the time-domain, and is shielded from Fourier domain spectral leakage caused by red timing noise or irregular sampling. The Bayesian pipeline can be incorporated into a more general pipeline which simultaneously estimates pulsar noise properties and other stochastic signals.

The injection code we use corresponds to a modified version of the code included in the PAL2 library,⁷ allowing complete control over noise and signal characteristics. For

a fiducial source, we are only interested in sensible binary parameters which will illustrate the efficacy of the search pipeline. We consider a source with the following characteristics: $\{\mathcal{M} = 10^9 M_\odot, F = 5 \text{ nHz}, \phi = 1.0, \theta = 1.1, \iota = 0.0, l_0 = 0.5, \psi = 0.5, \gamma = 0.5\}$, and a luminosity distance scaled by demanding the optimal SNR for the source is 20. This SNR is rather large, but will illuminate the presence of any systematic biases when the statistical errors are small. We will consider both a circular binary system ($e = 0$) and a moderately eccentric one ($e = 0.5$).

We search for binary parameters by stochastically sampling parameter space with a package which employs several advanced MCMC techniques.⁸

6. RESULTS

6.1. Bayesian pipeline

We accelerate the generation of templates for the GW-induced residuals by making the number of waveform harmonics adapt based on the current proposed eccentricity. As discussed in Sec. 2, the number of harmonics to adequately describe a binary with $e = 0.5$ is ~ 10 , whilst for $e = 0.9$ it is ~ 100 . Adaptation of the number of harmonics avoids template generation being the main computational bottleneck in our pipeline.

A triangle plot showing the 1D and 2D marginalized posterior PDFs for the main parameters of interest is shown in Fig. 6, with $\{68\%, 95\%, 99.7\%\}$ Bayesian credible region contours shown in the 2D PDFs. The injected values of parameters are shown with intersecting blue lines in the 2D PDFs and vertical blue lines in the 1D PDFs, where the simulated data contained a signal from an $e = 0.5$ binary. The posterior PDFs from our pipeline are completely consistent with the injected parameters, although we are unable to break the mass-distance degeneracy since we lack the extra lever-arm of the pulsar term in this Earth-term-only analysis. To illustrate the successful pipeline performance further, we overlay the 95% envelope of credible post-fit GW-induced residuals on top of the raw post-fit residuals from a single pulsar in our array. The results are shown for an $e = 0$ and $e = 0.5$ binary signal in Fig. 7, where we see that the region of credible residuals (enclosed within red dashed lines) tracks the main features in the raw post-fit residuals, and correctly interprets high frequency behavior around MJD 55100 in the right panel ($e = 0.5$) as binary periastris. In Fig. 7 we also show the deviation of the recovered residuals from the true injected residuals, where the envelope of credible residuals encompasses the line of zero offset. This shows that, even in this high SNR case, any systematic bias from the adaptation of the number of harmonics is very small, and our pipeline is robustly recovering the signal characteristics.

One might expect that distinctive high-frequency features due to periastris passage may improve the prospects for detection. We investigate this by computing the optimal SNR for a binary with varying orbital frequency, and a PTA timing baseline of 10 years. We draw the angular waveform parameters randomly and average over the resulting SNRs. The result of this procedure as a function of binary eccentricity is shown in Fig. 8, where we see a transition in behavior as the binary orbital frequency moves through the most sensitive location in the pulsar-timing band. From theoretical calculations and analysis of real data (Moore et al. 2015; Yardley et al. 2010;

⁵ For examples and some discussion, see the appendices of Arzoumanian et al. (2014).

⁶ http://www.ipta4gw.org/?page_id=89

⁷ <https://github.com/jellis18/PAL2>

⁸ <https://github.com/jellis18/PTMCMCSampler>

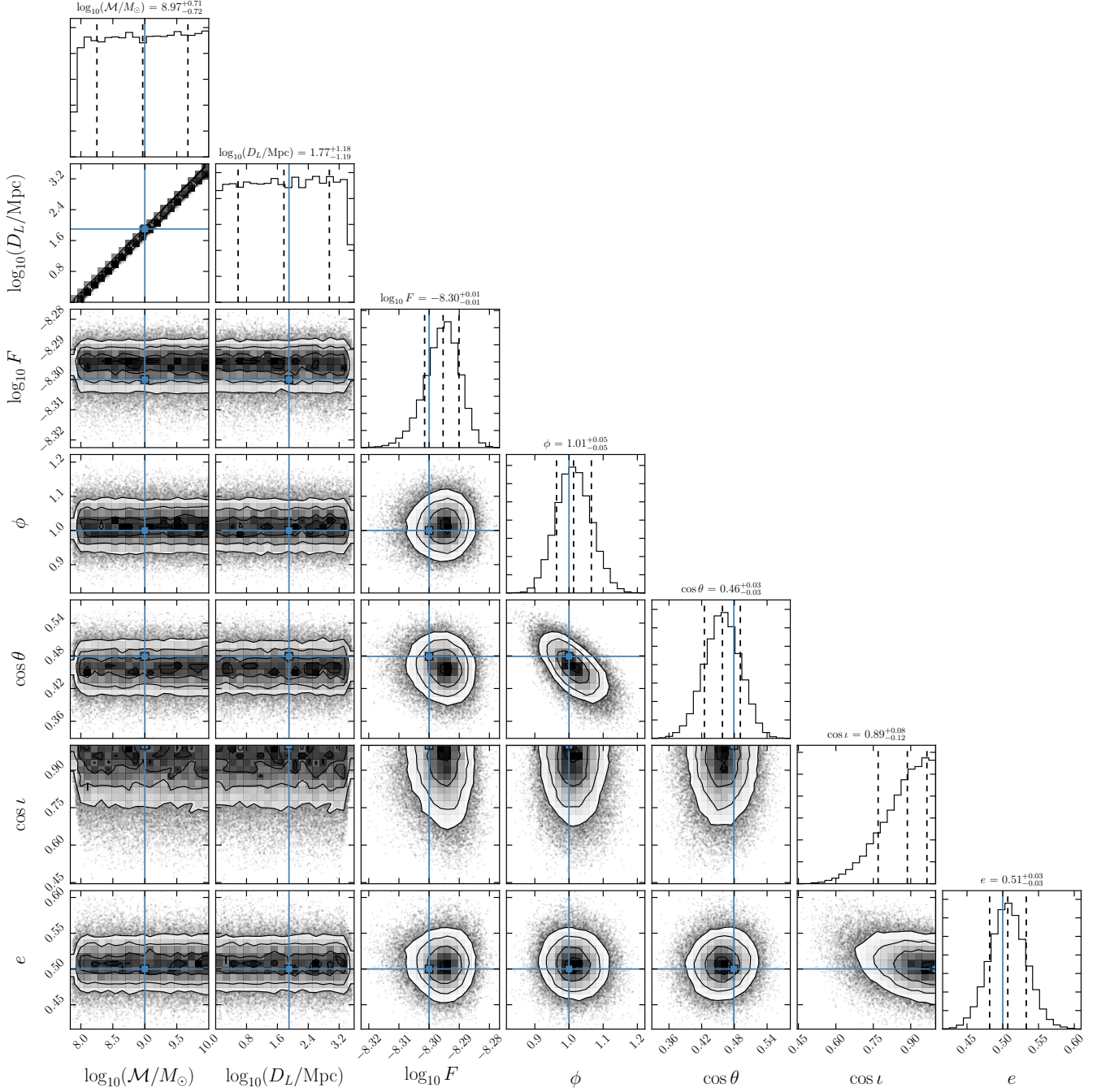


Figure 6. A triangle plot (Foreman-Mackey et al. 2014) showing 1D and 2D marginalized posterior PDFs for the main parameters of interest in a Bayesian single-source search on an $e = 0.5$ dataset. Contours corresponding to $\{68\%, 95\%, 99.7\}\%$ Bayesian credible regions are shown in the 2D PDFs, whilst the mean recovered parameters with 1σ error bars are shown in the 1D PDFs. Injected parameters are shown with intersecting blue lines in the 2D PDFs and vertical blue lines in the 1D PDFs. The recovered posterior PDFs are completely consistent with the injected parameters.

Arzoumanian et al. 2014), we expect the region of peak PTA sensitivity to a continuous GW to be at a GW frequency of $\sim 1/T - 2/T$, while sensitivity is inhibited at lower frequencies by fitting of the pulsar quadratic spindown parameters in its timing-model, and higher frequencies are dominated by white TOA measurement errors. For $e = 0$ binary signals in this simulated PTA, this peak corresponds to an orbital frequency of $\sim 1.6 - 3.2$ nHz, which is verified numerically in Fig. 9. In Fig. 8 we see that at higher eccentricities the SNR is enhanced when the injected orbital frequency lies below

1 nHz, and diminished when it lies above 5 nHz. We can make sense of this by recalling the spectral decomposition of the variance of the GW-induced residuals shown in Fig. 4, where as the eccentricity is increased the variance is distributed amongst higher harmonics of the orbital frequency. For systems with $F \lesssim 1$ nHz this will enhance the SNR since power in the residual variance is shifted into the region of peak PTA sensitivity, while for systems with $F \gtrsim 5$ nHz this diminishes the SNR since the power in the residual variance is distributed into higher, less sensitive frequencies of the PTA

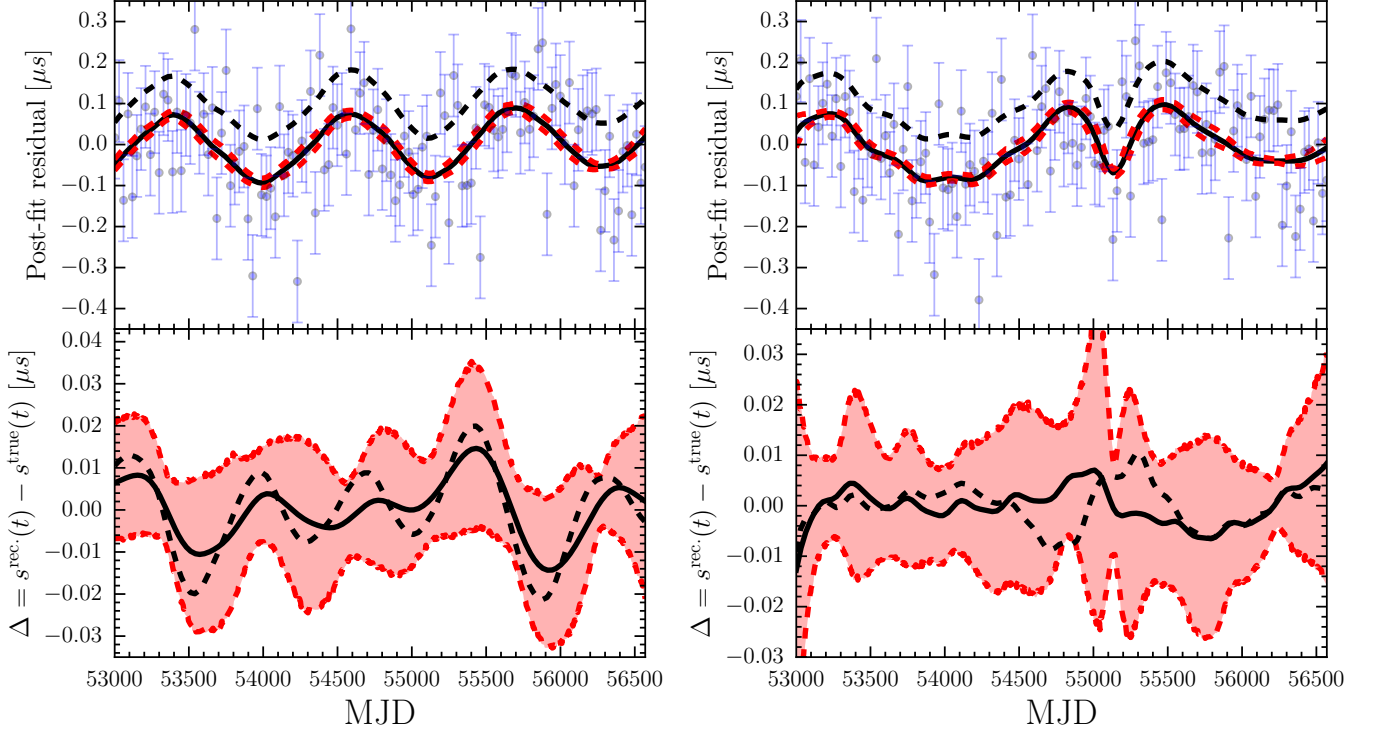


Figure 7. The post-fit residuals of pulsar J0030+0451 for simulated data are shown in the upper portions of both panels as blue points with associated error bars. The left panel corresponds to an injected GW signal from a circular ($e = 0.0$) binary, while the right panel corresponds to an injected GW signal from an $e = 0.5$ binary. (Upper): The boundaries of the 95% credible envelope of post-fit residuals induced by the GWs are shown as red dashed lines, while the residuals corresponding to the mean signal parameters are shown as solid black. These GW residuals are computed from the parameter posterior PDFs returned by Bayesian analysis of the simulated data, and then projected to post-fit values (Demorest et al. 2013). The black dashed line shows the maximum likelihood post-fit residuals returned by an eccentric \mathcal{F}_e -statistic (see Sec. 6.2) analysis (residuals are offset by $+0.1 \mu\text{s}$ for ease of viewing). (Lower): The offset of the reconstructed GW-induced residuals from the injected residuals is shown, where all lines correspond to the same cases as the upper panels. The boundaries of the 95% Bayesian credible envelope of post-fit residuals encompasses $\Delta = 0$, which is a good indicator of the robustness of the pipeline.

Table 1

Matched-filtering SNR of Bayesian maximum *a posteriori* templates and \mathcal{F}_e -statistic maximum likelihood templates for different injected signals, with the latter in parentheses. The signals are injected with an optimal SNR of 20.

		Injected signal	
		$e = 0.0$	$e = 0.5$
Modeled signal	Circular	19.86 (19.87)	16.09 (16.10)
	Eccentric	19.89 (19.87)	20.54 (20.60)

band.

We now address the detection penalty one might incur by searching for an eccentric binary signal with a circular waveform model, which was also investigated in Zhu et al. (2015). Firstly, we compute the matched-filtering SNR of the maximum *a posteriori* signals from Bayesian analysis of $e = \{0.0, 0.5\}$ datasets, where we either model the binary signal as eccentric or circular. The results are shown in Table 1, where we observe a $\sim 20\%$ reduction in SNR when a circular waveform model is applied to a binary signal with $e = 0.5$. We now investigate this more rigorously for a variety of binary frequencies and eccentricities. We compute the matched-filtering SNR for a circular (monochromatic) template in data with an eccentric signal, and compare this to the optimal SNR of the same eccentric signal. The resulting statistic, $\rho_{\text{circ}}/\rho_{\text{opt}}$, is a measure of the *effectualness* of the circular template in

representing the eccentric signal (Buonanno et al. 2009). At each eccentricity, the SNR is averaged over 10^3 binary orientations and locations, and maximized over the frequency of a monochromatic template. The matched-filtering SNR is computed in three different ways: (a) as a coherent SNR for the entire pulsar array, maximized over the monochromatic template frequency; (b) as a coincident SNR, with the SNR in each pulsar independently maximized over the monochromatic template frequency, and then added in quadrature to give the full array statistic; (c) as a coincident SNR, with the SNRs added in quadrature to give the full array statistic, but demanding a common frequency for the monochromatic template.

Our results are shown in Fig. 10 for orbital frequencies beyond the region of peak PTA sensitivity ($\gtrsim 5 \text{ nHz}$). For cases (a) and (b), the favored monochromatic template frequency is twice the orbital frequency until $e \sim 0.5 - 0.6$, and incurs an increasingly harsh SNR penalty as the eccentricity of the signal is increased. However, beyond $e \sim 0.5 - 0.6$ the SNR recovers slightly, since the template frequency now favors the fundamental harmonic of the signal, which is lower and closer to the region of peak PTA sensitivity. This is seen even more clearly in case (c), where there is a common monochromatic template frequency across all pulsars when constructing the coincident SNR. The loss in SNR is slightly greater in (a) than in (b) and (c), since in the former we require signal coherence amongst all pulsars in the array. The behaviour found for these three cases is likely pessimistic, since in real matched-

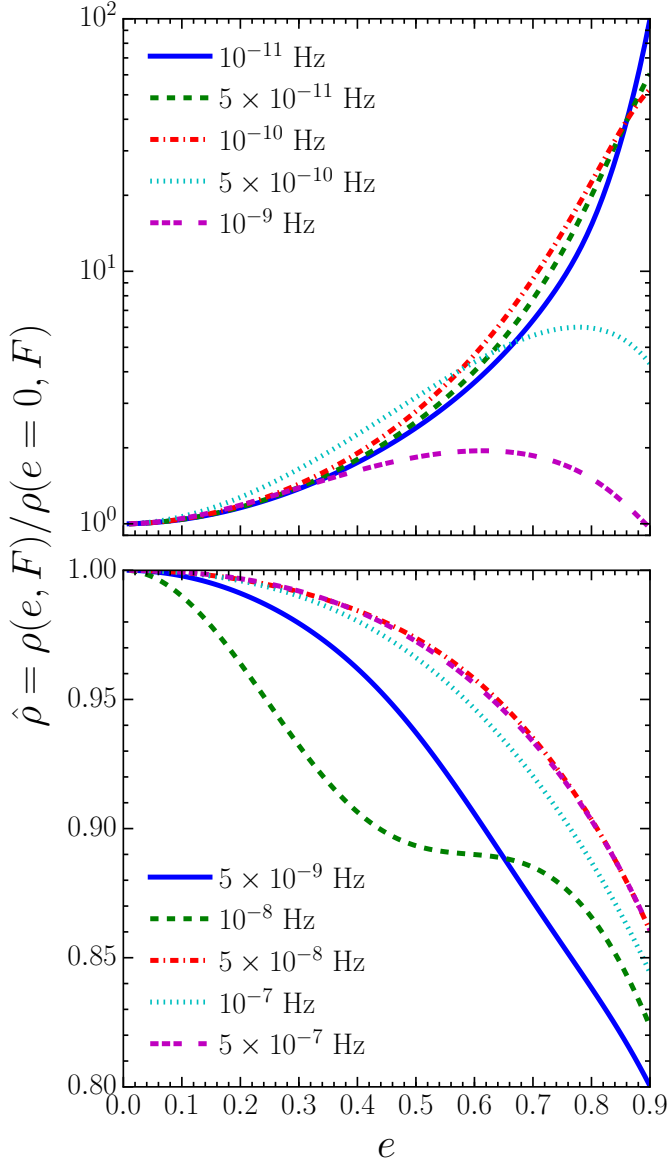


Figure 8. Normalized optimal SNR of a single source as a function of the binary eccentricity for a PTA timing baseline of 10 years. Only the Earth-term component is considered. Each curve corresponds to a different choice of binary orbital frequency, and is computed by averaging the SNR over all waveform angular parameters. For reference, the GW frequency of greatest sensitivity in this pulsar array is ~ 5 nHz.

filtering searches the SNR is maximized over all template parameters rather than just the frequency. Lower orbital frequency SNR curves exhibit similarly increasing penalties as the eccentricity is raised, but the trends are not as smooth. Future studies should extend the circular template investigations presented here and in [Zhu et al. \(2015\)](#) to perform realistic signal injections and recoveries for many binary eccentricities and orbital frequencies.

6.2. Eccentric \mathcal{F}_e statistic

We wish to construct a form of the \mathcal{F}_e statistic ([Babak & Sesana 2012](#); [Ellis et al. 2012](#)) which can be applied to GW signals from binaries with arbitrary eccentricity. In practice, as in the rest of this paper, we only consider systems with $e \in [0, 0.9]$. The \mathcal{F}_e statistic as it is constructed in [Ellis et al.](#)

(2012) is a maximum-likelihood estimator of the source’s sky-location and orbital frequency, and requires that the expression for the induced residuals be rearranged into a form which permits maximization of the likelihood-ratio over the coefficients of a set of time-dependent basis-functions. The likelihood-ratio, Λ , is defined as the ratio of the likelihood of the data in a model which includes a signal to the noise-only null hypothesis:

$$\begin{aligned} \ln \Lambda &= \ln \left[\frac{\mathcal{L}(\mathbf{s}|\delta\mathbf{t})}{\mathcal{L}(\mathbf{0}|\delta\mathbf{t})} \right] \\ &= (\delta\mathbf{t}|\mathbf{s}) - \frac{1}{2}(\mathbf{s}|\mathbf{s}). \end{aligned} \quad (37)$$

We extend the \mathcal{F}_e statistic by rewriting the Earth term residuals (in a single pulsar) given by Eqs. (21) and (22) as:

$$s(t) = \sum_{i=1}^6 w_i \mathcal{W}^i, \quad (38)$$

where,

$$\begin{aligned} w_1 &= \zeta \left[- (1 + \cos^2 \iota) \cos(2\gamma) \cos(2\psi) + 2 \cos \iota \sin(2\gamma) \sin(2\psi) \right], \\ w_2 &= \zeta \left[(1 + \cos^2 \iota) \sin(2\gamma) \cos(2\psi) + 2 \cos \iota \cos(2\gamma) \sin(2\psi) \right], \\ w_3 &= \zeta \left[(1 - \cos^2 \iota) \cos(2\psi) \right], \\ w_4 &= \zeta \left[(1 + \cos^2 \iota) \cos(2\gamma) \sin(2\psi) + 2 \cos \iota \sin(2\gamma) \cos(2\psi) \right], \\ w_5 &= \zeta \left[- (1 + \cos^2 \iota) \sin(2\gamma) \sin(2\psi) + 2 \cos \iota \cos(2\gamma) \cos(2\psi) \right], \\ w_6 &= \zeta \left[- (1 - \cos^2 \iota) \sin(2\psi) \right], \end{aligned} \quad (39)$$

$$\begin{aligned} \mathcal{W}^1 &= \tilde{F}^+(\hat{\Omega}) \omega^{-1/3} \sum_n x_{a_n} \sin[n\omega(t-t_0) + nl_0], \\ \mathcal{W}^2 &= \tilde{F}^+(\hat{\Omega}) \omega^{-1/3} \sum_n x_{b_n} \cos[n\omega(t-t_0) + nl_0], \\ \mathcal{W}^3 &= \tilde{F}^+(\hat{\Omega}) \omega^{-1/3} \sum_n x_{c_n} \sin[n\omega(t-t_0) + nl_0], \\ \mathcal{W}^4 &= \tilde{F}^\times(\hat{\Omega}) \omega^{-1/3} \sum_n x_{a_n} \sin[n\omega(t-t_0) + nl_0], \\ \mathcal{W}^5 &= \tilde{F}^\times(\hat{\Omega}) \omega^{-1/3} \sum_n x_{b_n} \cos[n\omega(t-t_0) + nl_0], \\ \mathcal{W}^6 &= \tilde{F}^\times(\hat{\Omega}) \omega^{-1/3} \sum_n x_{c_n} \sin[n\omega(t-t_0) + nl_0], \end{aligned} \quad (40)$$

and we adapt the number of terms in these summations based on the binary eccentricity. This is the same adaptation as discussed in the previous section for the Bayesian analysis.

The antenna pattern functions $\tilde{F}^A(\hat{\Omega})$ are related to $F^A(\hat{\Omega})$ by,

$$\begin{pmatrix} F^+ \\ F^\times \end{pmatrix} = \begin{pmatrix} \cos(2\psi) & -\sin(2\psi) \\ \sin(2\psi) & \cos(2\psi) \end{pmatrix} \begin{pmatrix} \tilde{F}^+ \\ \tilde{F}^\times \end{pmatrix}. \quad (41)$$

The coefficients w_i are a function of *extrinsic* source parameters $\{\zeta, \iota, \psi, \gamma\}$, whilst the time-dependent basis-functions \mathcal{W}^i are a function of *intrinsic* source parameters $\{F, \theta, \phi, e, l_0\}$.

Hence, the full PTA signal template can be written as:

$$\mathbf{s}(t) = \sum_{i=1}^6 w_i \mathbf{W}^i(t), \quad (42)$$

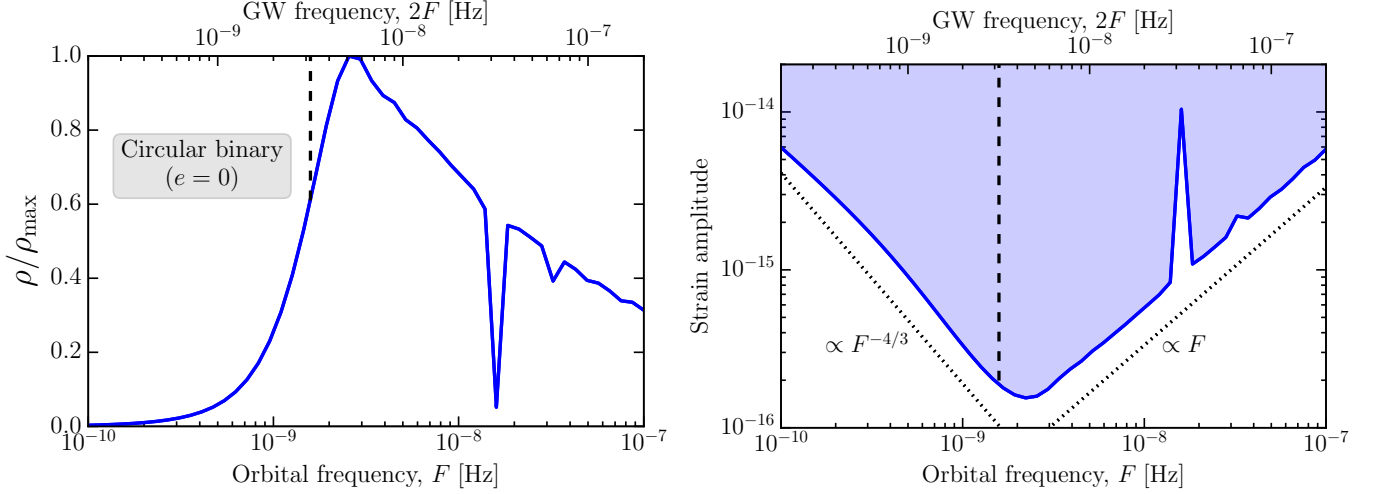


Figure 9. (Left): Optimal SNR of a circular binary GW signal in our fiducial pulsar-timing array. The SNR is normalized with respect to the maximum across orbital frequency. Since the binary is circular the GW emission is monochromatic with a frequency equal to twice the orbital frequency. The vertical black dashed line denotes the inverse observation timespan ($1/T \sim 3.2$ nHz). The two notches at high frequency occur at GW frequencies of ~ 32 nHz and ~ 63 nHz. The former occurs since we fit out the Earth's motion around the Sun to convert our observations to the SSB, and therefore lose sensitivity around 1/year. The latter occurs at a frequency of 2/year and arises from the timing parallax fitting of each pulsar's sky location. (Right): The optimal SNR can be inverted to determine the minimum strain amplitude $\zeta\omega^{2/3}$ in each frequency bin which has an SNR above or equal to a threshold, where $\rho_{\min} = 3$ in this example. The region of detectability is shaded blue.

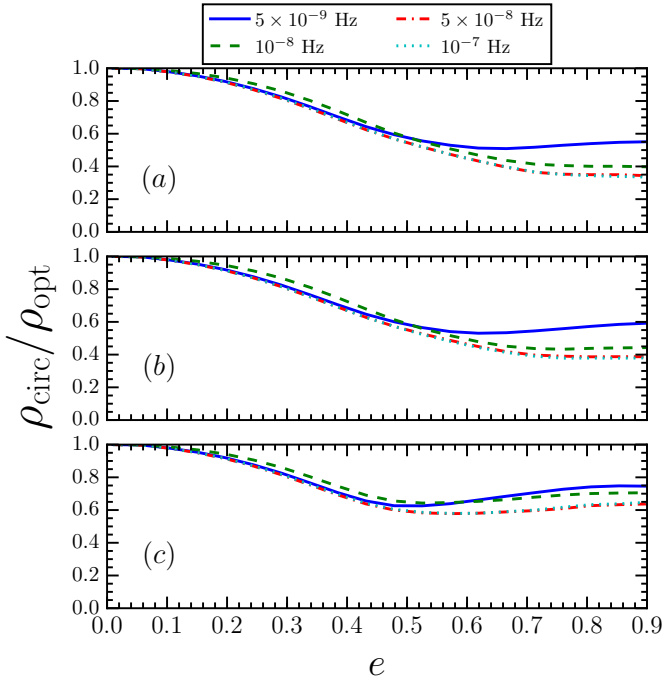


Figure 10. Ratio of circular-template matched-filtering SNR to optimal SNR for signals with various orbital frequencies and eccentricities. Case (a) shows results for a coherent array SNR. Case (b) shows results for a coincident array SNR with independently maximized template frequencies in each pulsar. Case (c) shows results for a coincident array SNR with a common monochromatic template frequency. Further details and discussion are provided in the text.

where,

$$\mathbf{W}^i = \begin{bmatrix} \mathcal{W}_1^i(t) \\ \mathcal{W}_2^i(t) \\ \vdots \\ \mathcal{W}_{N_p}^i(t) \end{bmatrix}, \quad (43)$$

and $\mathcal{W}_j^i(t)$ denotes the quantity \mathcal{W}^i defined by Eqs (40) for pulsar j . Inserting Eq. (42) into Eq. (37) and using Einstein summation convention, we have

$$\ln \Lambda = w_i N^i - \frac{1}{2} M^{ij} w_i w_j, \quad (44)$$

where $N^i = (\delta \mathbf{t} | \mathbf{W}^i)$ and $M^{ij} = (\mathbf{W}^i | \mathbf{W}^j)$. By maximizing the log-likelihood ratio over the amplitude coefficients, w_i , we get their maximum-likelihood values:

$$\hat{w}_i = M_{ij} N^j, \quad (45)$$

where $M_{ij} = (M^{ij})^{-1}$.⁹ Substituting these coefficients back into the expression for $\ln \Lambda$ gives the eccentric \mathcal{F}_e statistic:

$$\mathcal{F}_e = \frac{1}{2} N^i M_{ij} N^j. \quad (46)$$

The procedure to estimate the maximum likelihood values of all of the signal parameters is as follows:

- We find the local maxima of the \mathcal{F}_e statistic in the space of intrinsic parameters via a straightforward function maximization, or we can map out the distribution with an MCMC analysis and determine the maximum likelihood point from the chain.
- The intrinsic parameters which maximize the \mathcal{F}_e statistic can be used to compute the quantities M_{ij} and N^i , which are combined to determine the maximum likelihood coefficients, w_i , via Eq. (45).
- From these coefficients, we obtain a maximum likelihood estimate of the physical extrinsic parameters, as described below.

There are six w_i parameters, but these are functions of only four physical extrinsic parameters and so not all combinations

⁹ Through practical experience we find that the inverted matrix has greater numerical stability at low eccentricity ($e \lesssim 0.05$) when a Moore-Penrose pseudoinverse is used, with a typical singular value cutoff of $\sim 10^{-10}$.

of w_i 's correspond to physical systems. However, we can obtain extrinsic parameter estimates from estimates of the w_i 's following (Cornish & Porter 2007). We define

$$\begin{aligned} A_+ &= \sqrt{(w_1+w_5)^2 + (w_2-w_4)^2} + \sqrt{(w_1-w_5)^2 + (w_2+w_4)^2}, \\ A_\times &= \sqrt{(w_1+w_5)^2 + (w_2-w_4)^2} - \sqrt{(w_1-w_5)^2 + (w_2+w_4)^2}, \end{aligned} \quad (47)$$

and

$$A = A_+ + \sqrt{A_+^2 - A_\times^2}. \quad (48)$$

By employing the quantities $\{A_+, A_\times, A\}$ we can map from $w_{i \in [1,6]}$ to $\{\zeta, \iota, \psi, \gamma\}$ with the following manipulations:

$$\begin{aligned} \zeta &= \frac{A}{4}, \\ \cos \iota &= -\frac{A_\times}{A}, \\ \tan(2\psi) &= \frac{A_\times w_1 - A_+ w_5}{A_\times w_4 + A_+ w_2}, \\ \tan(2\gamma) &= \frac{A_\times w_1 - A_+ w_5}{A_+ w_4 + A_\times w_2}. \end{aligned} \quad (49)$$

This procedure was carried out for the simulated data which was previously analyzed by the Bayesian pipeline in Sec. 6.1. We use parallel-tempering MCMC to map out the \mathcal{F}_e statistic distribution over the intrinsic parameter space. From this MCMC chain we determine the maximum-likelihood intrinsic parameters, which are then used to construct w_i via Eq. (45). Having the maximized w_i and corresponding \mathcal{W}^i , we now compute the maximum-likelihood timing residuals induced by the GWs from an eccentric binary. The results for an $e = 0$ and $e = 0.5$ binary signal are shown in Fig. 7, where the maximum-likelihood GW-induced post-fit residuals are overlaid as black dashed lines on top of the raw post-fit residuals from pulsar J0030+0451, showing excellent tracking of the residual behavior and good agreement with the Bayesian recovery. Note that these maximum-likelihood residuals are offset by $+0.1 \mu\text{s}$ for ease of viewing.

7. CAVEATS & FUTURE DIRECTIONS

The analysis and results presented in this paper have relied on several assumptions. We discuss these here, and the prospects for relaxing these caveats in future work.

7.1. Prospects for including the pulsar term

In the majority of this paper, we have ignored a full treatment of the pulsar term signal. Since the pulsar term is retarded with respect to the Earth term, it will represent the binary at an earlier stage of its orbital evolution, with a larger eccentricity and smaller orbital frequency. It is now well known that the pulsar term aids detection prospects for continuous wave sources, and is crucial in breaking degeneracies between the binary mass and its luminosity distance by providing extra information from the binary's evolution over the lag time between the Earth and pulsar term signals (Corbin & Cornish 2010; Lee et al. 2011; Ellis 2013).

Being able to model the orbital evolution of the binary, and constrain the properties of this evolution through continuous GW searches with PTAs, will provide a unique opportunity to probe the influence of other non-GW driving mechanisms. For example, the rate at which the binary orbital frequency, F , is driven by GWs, stellar scattering, and circumbinary disk interactions, scales as $\propto F^{11/3}$, $\propto F^{1/3}$, $\propto F^{4/3}$, respectively

(Sesana 2013). If we can include parametrized models of the rate of binary evolution in constructing full Earth and pulsar term signal models in a Bayesian or frequentist search, then we will be able to make statements about the relative importance of the aforementioned mechanisms. This in itself may provide clues as to how binaries are driven to sub-parsec orbital separations after dynamical friction in post-merger galaxies becomes inefficient, thereby adding to our knowledge of how the final parsec problem (Milosavljević & Merritt 2003) is ameliorated.

For now, we estimate the degree to which employing only the Earth term in searches is sub-optimal for detection. We compute the matched-filter SNR for an Earth term template applied to a full signal (including the pulsar term), and compare this to the optimal SNR for the full signal. In constructing the pulsar term component of the signal, we evolve the orbital parameters of the binary backwards in time according to Eq. (6) and the procedure outline in Sec. 4, where we assume all pulsars lie at a distance of 1 kpc from the Earth. We assume all orbital evolution is GW driven. No pericenter-direction evolution or orbital-plane precession is considered, and we do not evolve the binary during the pulsar observation timespan of 10 years. To ease the computational burden, we use a sub-array of 6 pulsars spread across the sky, averaging the SNR over 10^3 binary locations and orientations.

The results are shown in Table 2 for a variety of Earth term orbital frequencies and eccentricities. As the orbital frequency and chirp mass are increased, the ratio of the Earth term SNR to the full SNR tends to grow with eccentricity. This is because higher mass, frequency, and eccentricity binaries are driven rapidly via GW emission, which in the most extreme cases leads to signals with pulsar term frequencies which are so far below the PTA sensitivity band that an Earth term template becomes an excellent approximation to the full signal. Even at fixed orbital frequency and eccentricity, the effect of increasing binary chirp mass is to raise the efficacy of an Earth term only template. However, care must be taken in the intermediate case, when we have moderate eccentricities, frequencies, and masses, which generate pulsar term signals that remain in the PTA band, and whose spectrum of GW frequencies may exceed the fundamental harmonic of the Earth term signal. The worst matches between signal and template occur for low mass, low eccentricity systems with orbital frequencies close to the region of peak PTA sensitivity (~ 5 nHz) – the combination of high array sensitivity and negligible orbital evolution leads to pulsar term signals close to this region of peak sensitivity, and thus very poor matches (which are sometimes negative since we employ a coherent SNR). In general, the pulsar term increases the signal detection prospects, but confusion may arise between different harmonics in the Earth and pulsar terms, which would harm parameter estimation efforts. So long as the Earth and pulsar terms remain distinguishable, we will learn more about the system parameters from the pulsar term's inclusion. Future work should study the prospects for incorporating the pulsar term in eccentric binary search strategies, and investigate the rich science that can be mined from having access to snapshots of the binary evolution from thousands of years in its past.

7.2. Binary orbital evolution during the observation timespan

We now test the assumption of binary non-evolution over typical PTA observation timespans. For different initial Earth

Table 2

The matched-filter SNR for an Earth term template is compared against the optimal full signal SNR to construct $\rho_{\text{earth}}/\rho_{\text{full}}$. At each Earth term orbital frequency and eccentricity, we evolve a binary backwards in time by $L(1 + \hat{\Omega} \cdot \hat{u})$ to construct the pulsar term waveform, where $L = 1$ kpc for all pulsars.

Orbital frequency [nHz]	Eccentricity															
	$e = 0.0$				$e = 0.25$				$e = 0.50$				$e = 0.75$			
	$\mathcal{M} [M_{\odot}]$				$\mathcal{M} [M_{\odot}]$				$\mathcal{M} [M_{\odot}]$				$\mathcal{M} [M_{\odot}]$			
	10^7	10^8	10^9	10^{10}	10^7	10^8	10^9	10^{10}	10^7	10^8	10^9	10^{10}	10^7	10^8	10^9	10^{10}
0.1	0.76	0.76	0.76	0.76	0.73	0.73	0.73	0.73	0.51	0.51	0.51	0.51	0.12	0.12	0.12	0.12
0.5	0.78	0.78	0.78	0.78	0.66	0.66	0.66	0.66	0.33	0.33	0.33	0.34	0.15	0.15	0.16	0.41
1.0	0.63	0.63	0.63	0.64	0.47	0.47	0.47	0.49	0.25	0.25	0.25	0.36	0.10	0.10	0.16	0.76
5.0	-0.03	-0.03	0.07	0.65	-0.02	-0.02	0.13	0.72	0.0	0.01	0.38	0.87	0.02	0.16	0.81	0.99
10.0	-0.01	0.02	0.59	0.62	-0.03	0.01	0.6	0.73	-0.04	0.10	0.64	0.93	0.03	0.50	0.87	1.0
50.0	0.21	0.68	0.63	0.42	0.3	0.68	0.56	0.95	0.53	0.67	0.81	0.99	0.68	0.66	0.99	1.0
100.0	0.66	0.65	0.55	0.34	0.67	0.64	0.65	0.99	0.68	0.52	0.93	1.0	0.64	0.81	0.99	1.0

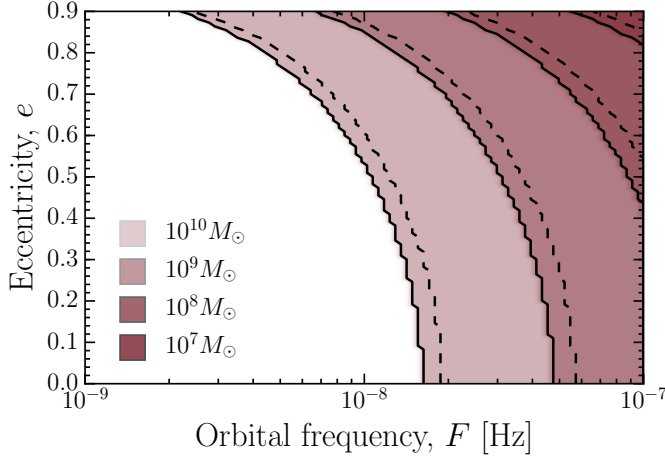


Figure 11. Exclusion regions in binary eccentricity and orbital frequency as a function of *chirp mass*, corresponding to parameter combinations where the fundamental (dashed black lines) and second harmonic (solid black lines on the boundary of shaded exclusion regions) of the orbital frequency evolve during $T = 10$ years by more than the PTA frequency resolution, $\Delta f = 1/T = 3.2$ nHz, rendering the assumption of binary non-evolution invalid.

term parameter choices $\{\mathcal{M}, F, e\}$, we numerically evolve a binary forward in time by 10 years according to Eq. (6). Figure 11 shows exclusion regions in parameter space where the fundamental and second harmonic of the orbital frequency evolve by more than the PTA frequency resolution, $\Delta f = 1/T = 3.2$ nHz, which may render the approximation of binary non-evolution within our observing window invalid. The second harmonic will dominate the signal for low eccentricities whilst the fundamental harmonic will dominate at higher eccentricities.

A more rigorous way of testing this is to investigate how this assumption affects our ability to perform parameter estimation. If the non-evolution model performs well within the range of expected SNR, such that the systematic bias introduced via our assumption of binary non-evolution is smaller than statistical errors, then we can judge the model to be an excellent functioning approximation. More formally, we want to satisfy the *indistinguishability criterion* (Cutler & Vallisneri 2007; Creighton & Anderson 2012):

$$(\delta s(t) | \delta s(t)) < 1, \quad (50)$$

where $\delta s(t)$ corresponds to the difference between the approximated residuals in the non-evolution model and the true residuals. Satisfying the inequality in Eq. (50) approximately corresponds to the systematic errors arising from modeling

bias being smaller than statistical measurement errors. The tolerance SNR, ρ_{tol} , above which systematic errors from insufficient template accuracy may exceed statistical measurement errors, and thus become problematic, is given by

$$\rho_{\text{tol}}^2 = \frac{(\mathbf{s}(t) | \mathbf{s}(t))}{(\delta \mathbf{s}(t) | \delta \mathbf{s}(t))}, \quad (51)$$

where $\mathbf{s}(t)$ are the true residuals (concatenated over all pulsars) induced by a binary which may be evolving over our observation timespan. To compute this, we numerically evolve the orbital parameters of a binary over 10 years using Eq. (6), with varying choices of initial orbital frequency and eccentricity. The evolved orbit is then used to compute the pulse redshift and (via numerical integration) the GW-induced timing residual at each pulse TOA. The typical ratio of the time required to compute the GW signal numerically versus analytically is $\sim \mathcal{O}(10^4)$, which is why a fully numerical approach is clearly intractable at present.

The tolerance SNR is shown in Fig. 12 as a function of binary eccentricity, orbital frequency, and chirp mass. We choose a cutoff value of the tolerance SNR equal to 10 since this may correspond to realistic values of the SNRs of first PTA detections of single GW sources after ~ 10 years of IPTA and SKA1 activity (Rosado et al. 2015). If our model can be successfully applied to real signals above this cutoff value, then we conclude that the treatment used in this paper is valid well into the era of first PTA detections. We see that at a binary chirp mass of $10^8 M_{\odot}$ the tolerance SNR is above 10 for most frequencies and eccentricities, indicating that the assumption of non-evolution is valid. The approximation begins to break down at higher eccentricities and frequencies ($\gtrsim 5 \times 10^{-8}$ Hz) where the rate of binary evolution is higher. At $10^9 M_{\odot}$ our model is appropriate at all eccentricities for frequencies lower than 10^{-8} Hz, however the tolerance SNR for $F = 10^{-8}$ Hz drops below cutoff at $e \sim 0.7$, and at higher frequencies the assumption of binary non-evolution is inappropriate. Finally, for the most massive binaries with $\mathcal{M} = 10^{10} M_{\odot}$, the tolerance SNR remains above cutoff for orbital frequencies lower than 5×10^{-9} Hz at all eccentricities, while at 5×10^{-9} Hz the tolerance SNR only drops below 10 at $e \sim 0.6$.

Therefore, our assumption (which has been shared by all other authors in this field) of binary non-evolution over typical PTA timing baselines is appropriate for most frequencies at or below the region of peak PTA sensitivity. The approximation only begins to break down for the most massive systems above orbital frequencies of $\sim 5 \times 10^{-9}$ Hz and eccentricities of 0.6, allowing the signal model and analysis techniques

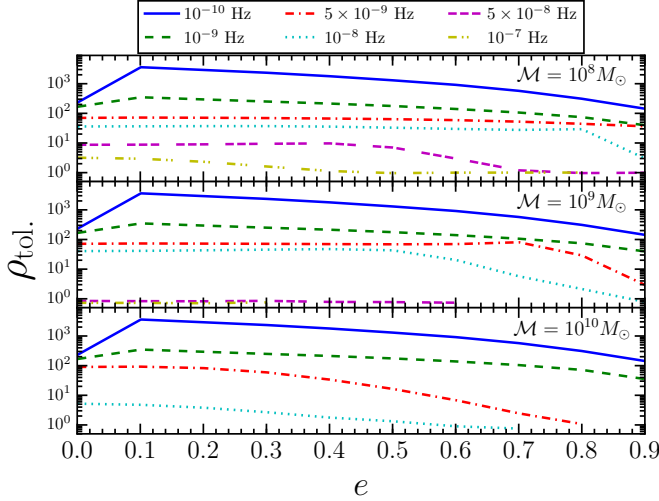


Figure 12. The tolerance SNR, ρ_{tol} , for a range of binary eccentricities, orbital frequencies, and chirp masses is shown. This indicates the SNR above which systematic parameter errors (which occur by keeping binary parameters fixed over the 10 year PTA timing baseline) may exceed statistical measurement errors.

developed in this article to be applied to real data with robust outcomes. Future studies are required to investigate faster and more tractable strategies for modeling the orbital evolution of high mass, high frequency, and high eccentricity binaries over PTA timing baselines.

8. CONCLUSIONS

PTAs are uniquely suited to explore the dynamical evolution of SMBH binaries before and after they decouple from their astrophysical environments to become dominated by GW emission. An increasing number of studies tend to suggest that the mechanisms that may drive SMBH binaries to small orbital separations could also lead to an increase in binary eccentricity that will be detectable in the frequency band of PTAs. Extracting this information from real data will substantially increase our understanding of the mechanisms that lead to the formation, hardening and eventual coalescence of SMBH binaries. In this article we have introduced several tools to address this issue. We have developed a robust, accurate and computationally efficient Bayesian pipeline to explore the feasibility of detecting and reconstructing the astrophysical parameters of eccentric SMBH binaries in PTA data, and have developed for the first time an eccentric \mathcal{F}_e -statistic that is, by construction, suitable to study systems of arbitrary eccentricity.

We have used these tools to determine the accuracy with which a simulated eccentric signal could be reconstructed, and have conclusively shown that the recovered and injected parameters are completely consistent. We have also shown that the automated waveform generation algorithm, which determines the number of harmonics needed to ensure that the modeled GW signal reproduces the full numerical solution with an accuracy better than 99.999%, prevents computational inefficiencies in the pipeline.

The influence of binary eccentricity on PTA single-source detection prospects was also considered. Assuming that the sensitivity peak of a PTA to continuous wave sources is located at a GW frequency f_0 , we have shown that eccentricity will enhance the detection prospects of SMBH binaries with orbital frequencies $\lesssim f_0$. This is because the signal spectrum

of eccentric binaries is distributed into higher harmonics of the orbital frequency than in the case of a circular binary, leading to components of the signal being located in the region of maximum PTA sensitivity. On the other hand, binaries with orbital frequencies $\gtrsim f_0$ will undergo an SNR attenuation because the signal power is shifted to higher frequencies where the PTA sensitivity is poorer and dominated by TOA measurement errors. In summary, systems with signals which are below band in the circular case get pushed into band through increasing eccentricity, while systems that are optimally located in frequency for the circular case get pushed out of band by eccentricity.

We found that applying a circular waveform model in the analysis of data with increasingly eccentric binary signals incurs an SNR penalty which grows with eccentricity, and is $\sim 60\%$ at worst case for coherent and coincident analyses. Future work is needed to perform realistic signal injections and recoveries at a variety of binary eccentricities and orbital frequencies to rigorously assess the penalty suffered when adopting a circular binary waveform model.

Several of the approximations used in the techniques presented in this article were briefly investigated. We found that for very high mass, frequency and eccentricity binaries, an Earth term signal model performs just as well as a full signal model incorporating the pulsar term, since the binary will have evolved so significantly that the pulsar term signal lies below band. Furthermore, the possible bias from assuming binary non-evolution over a PTA observation time of 10 years was studied, and was found to be unimportant for moderately massive and eccentric systems in the era of first PTA detections.

Huerta et al. (2015) and this article have provided a solid foundation to explore in a consistent way the influence of eccentricity on the detection and parameter estimation of SMBH binaries with PTAs. The tools presented in this article can be readily incorporated into all present and planned analysis pipelines. The toolkit introduced in these articles could be extended to explore in detail what constraints may be placed on the various astrophysical mechanisms that can drive the dynamical evolution of SMBH binaries prior to becoming dominated by GW emission.

APPENDIX

FOURIER ANALYSIS OF THE KEPLER PROBLEM

From elementary properties of the ellipse we have

$$r = \frac{a(1-e^2)}{1+e\cos\Phi}, \quad (\text{A1})$$

where r is the separation vector between binary components, a is the orbital semi-major axis, e is the orbital eccentricity, and Φ is the orbital phase. By comparing the right hand side of Eq. (A1) to that of Eq. (1) and manipulating, we get

$$\cos\Phi = \frac{\cos(u)-e}{1-e\cos(u)}, \quad (\text{A2})$$

$$\sin\Phi = (1-e^2)^{1/2} \frac{\sin(u)}{1-e\cos(u)}. \quad (\text{A3})$$

Our problem reduces to finding a Fourier series expansion of $\sin u$ and $\cos u$ in terms of the mean anomaly, l . We make use of Eq. (2) throughout the following derivations.

The general form of a Fourier series expansion of an arbitrary function, $f(x)$, of real variable x is

$$f(x) = \frac{a_0}{2} + \sum_{n=1}^{\infty} \left[a_n \cos\left(\frac{\pi n x}{P}\right) + b_n \sin\left(\frac{\pi n x}{P}\right) \right], \quad (\text{A4})$$

where $f(x)$ is assumed to be integrable on an interval $[x_0, x_0 + P]$, and outside the interval the function is periodic with period P . The Fourier coefficients of the expansion are given by

$$\begin{aligned} a_n &= \frac{2}{P} \int_{x_0}^{x_0+P} f(x) \cos\left(\frac{\pi n x}{P}\right) dx, \\ b_n &= \frac{2}{P} \int_{x_0}^{x_0+P} f(x) \sin\left(\frac{\pi n x}{P}\right) dx. \end{aligned} \quad (\text{A5})$$

Now, we note that $e \sin(u)$ is a real, odd function over the range $[-\pi, \pi]$, and hence can be expanded as

$$e \sin(u) = \sum_{n=1}^{\infty} b_n \sin(nl), \quad (\text{A6})$$

where

$$\begin{aligned} b_n &= \frac{2}{\pi} \int_0^{\pi} e \sin(u) \sin(nl) dl \\ &= \frac{2}{\pi} \left[-\frac{e}{n} \sin(u) \cos(nl) \right]_0^{\pi} + \frac{2}{n\pi} \int_0^{\pi} \cos(nl) \frac{d(e \sin(u))}{dl} dl \\ &= \frac{2}{n\pi} \int_0^{\pi} \cos(nl) \cdot (du - dl) \\ &= \frac{2}{n\pi} \int_0^{\pi} \cos(nl) du - \frac{2}{n\pi} \int_0^{\pi} \cos(nl) dl \\ &= \frac{2}{n\pi} \int_0^{\pi} \cos(nu - ne \sin(u)) du \\ &= \frac{2}{n} J_n(ne), \end{aligned} \quad (\text{A7})$$

and $J_n(x)$ is a Bessel function of the first kind. Thus

$$\sin(u) = \sum_{n=1}^{\infty} \frac{2}{ne} J_n(ne) \sin(nl). \quad (\text{A8})$$

The function $e \cos(u)$ is real and even over the range $[-\pi, \pi]$, and hence can be expanded as

$$e \cos(u) = \frac{a_0}{2} + \sum_{n=1}^{\infty} a_n \cos(nl), \quad (\text{A9})$$

where

$$\begin{aligned} a_0 &= \frac{2}{\pi} \int_0^{\pi} e \cos(u) dl \\ &= \frac{2}{\pi} \int_0^{\pi} e \cos(u) \frac{dl}{du} du \\ &= \frac{2}{\pi} \int_0^{\pi} e \cos(u) (1 - e \cos(u)) du \\ &= -e^2, \end{aligned} \quad (\text{A10})$$

and

$$\begin{aligned} a_n &= \frac{2}{\pi} \int_0^{\pi} e \cos(u) \cos(nl) dl \\ &= \frac{2}{\pi} \left[\frac{e}{n} \cos(u) \sin(nl) \right]_0^{\pi} - \frac{2}{n\pi} \int_0^{\pi} \sin(nl) \frac{d(e \cos(u))}{dl} dl \\ &= \frac{2}{n\pi} \int_0^{\pi} e \sin(u) \sin(nu - ne \sin(u)) du \\ &= \frac{2}{n\pi} \int_0^{\pi} \frac{d(\cos(nu - ne \sin(u)))}{d(ne)} du \\ &= \frac{2}{n} J'_n(ne), \end{aligned} \quad (\text{A11})$$

and prime denotes differentiation with respect to the argument of the Bessel function.

Finally, we have

$$\begin{aligned} \cos(u) &= -\frac{e}{2} + \sum_{n=1}^{\infty} \frac{2}{n} J'_n(ne) \cos(nl), \\ \sin(u) &= \sum_{n=1}^{\infty} \frac{2}{ne} J_n(ne) \sin(nl). \end{aligned} \quad (\text{A12})$$

Using $l = (u - e \sin(u))$ such that $du/dl = 1/(1 - e \cos(u))$, we can now write down analytic expressions for trigonometric quantities of the orbital phase in terms of the mean anomaly:

$$\begin{aligned} \cos \Phi &= \frac{d}{dl} [\sin(u) - eu], \\ &= \frac{d}{dl} [(1 - e^2) \sin(u) - le], \\ &= -e + \frac{2}{e} (1 - e^2) \sum_{n=1}^{\infty} J_n(ne) \cos(nl), \end{aligned} \quad (\text{A13})$$

and

$$\begin{aligned} \sin \Phi &= -(1 - e^2)^{1/2} \frac{d(\cos(u))}{dl}, \\ &= 2(1 - e^2)^{1/2} \sum_{n=1}^{\infty} J'_n(ne) \sin(nl). \end{aligned} \quad (\text{A14})$$

We can then use the identity $2J'_n(x) = (J_{n-1}(x) - J_{n+1}(x))$ (Watson 1995) to reduce Eq. (A14) to

$$\sin \Phi = (1 - e^2)^{1/2} \sum_{n=1}^{\infty} [J_{n-1}(ne) - J_{n+1}(ne)] \sin(nl). \quad (\text{A15})$$

This research was in part supported by SRT's appointment to the NASA Postdoctoral Program at the Jet Propulsion Laboratory, administered by Oak Ridge Associated Universities through a contract with NASA. JRG's work is supported by the Royal Society. We thank Justin Ellis for useful feedback on this manuscript, and Alberto Sesana for fruitful discussions. This work was supported in part by National Science Foundation Grant No. PHYS-1066293 and the hospitality of the Aspen Center for Physics. Copyright © 2015. All rights reserved.

- Anholm, M., Ballmer, S., Creighton, J. D. E., Price, L. R., & Siemens, X. 2009, *Phys. Rev. D*, 79, 084030
- Apostolatos, T. A., Cutler, C., Sussman, G. J., & Thorne, K. S. 1994, *Phys. Rev. D*, 49, 6274
- Arzoumanian, Z., et al. 2014, *Astrophys. J.*, 794, 141
- Babak, S., & Sesana, A. 2012, *Phys. Rev. D*, 85, 044034
- Barack, L., & Cutler, C. 2004, *Phys. Rev. D*, 69, 082005
- Berger, E. 2013, ArXiv e-prints
- Berger, E., Fong, W., & Chornock, R. 2013, *Astrophys. J. Lett*, 774, L23
- Book, L. G., & Flanagan, E. E. 2011, *Phys. Rev. D*, 83, 024024
- Buonanno, A., Iyer, B. R., Ochsner, E., Pan, Y., & Sathyaprakash, B. S. 2009, *Phys. Rev. D*, 80, 084043
- Chandrasekhar, S. 1983, *The mathematical theory of black holes* (Research supported by NSF. Oxford/New York, Clarendon Press/Oxford University Press (International Series of Monographs on Physics. Volume 69), 1983, 663 p.)
- Corbin, V., & Cornish, N. J. 2010, ArXiv e-prints
- Cornish, N. J., & Porter, E. K. 2007, *Classical and Quantum Gravity*, 24, 5729
- Creighton, J. D., & Anderson, W. G. 2012, *Gravitational-Wave Physics and Astronomy: An Introduction to Theory, Experiment and Data Analysis* (John Wiley & Sons)
- Cutler, C., & Vallisneri, M. 2007, *Physical Review D*, 76, 104018
- Demorest, P. B., et al. 2013, *The Astrophysical Journal*, 762, 94
- Ellis, J. A. 2013, *Classical and Quantum Gravity*, 30, 224004
- Ellis, J. A., Siemens, X., & Creighton, J. D. E. 2012, *Astrophys. J.*, 756, 175
- Finn, L. S. 2001, *Phys. Rev. D*, 63, 102001
- Foreman-Mackey, D., Price-Whelan, A., Ryan, G., Emily, Smith, M., Barbary, K., Hogg, D. W., & Brewer, B. J. 2014, *triangle.py v0.1.1*
- Foster, R. S., & Backer, D. C. 1990, *The Astrophys. J.*, 361, 300
- Gebhardt, K., et al. 2000, *Astrophys. J. Lett*, 543, L5
- Goldstein, H. 1950, *Classical mechanics* (Addison-Wesley World Student Series, Reading, Mass.: Addison-Wesley, 1950)
- Hobbs, G. 2013, *Classical and Quantum Gravity*, 30, 224007
- Huerta, E. A., McWilliams, S. T., Gair, J. R., & Taylor, S. R. 2015, ArXiv e-prints
- Hughes, S. A. 2009, *ARA&A*, 47, 107
- Hughes, S. A., & Blandford, R. D. 2003, *Astrophys. J. Lett*, 585, L101
- Jaffe, A. H., & Backer, D. C. 2003, *The Astrophys. J.*, 583, 616
- Janka, H.-T., Eberl, T., Ruffert, M., & Fryer, C. L. 1999, *Astrophys. J. Lett*, 527, L39
- Kormendy, J., & Richstone, D. 1995, *ARA&A*, 33, 581
- Kramer, M., & Champion, D. J. 2013, *Classical and Quantum Gravity*, 30, 224009
- Lee, K. J., Wex, N., Kramer, M., Stappers, B. W., Bassa, C. G., Janssen, G. H., Karuppusamy, R., & Smits, R. 2011, *MNRAS*, 414, 3251
- Lee, W. H., & Ramirez-Ruiz, E. 2007, *New Journal of Physics*, 9, 17
- Magorrian, J., et al. 1998, *AJ*, 115, 2285
- Manchester, R. N., & IPTA. 2013, *Classical and Quantum Gravity*, 30, 224010
- McLaughlin, M. A. 2013, *Classical and Quantum Gravity*, 30, 224008
- Metzger, B. D., & Berger, E. 2012, *Astrophys. J.*, 746, 48
- Milosavljević, M., & Merritt, D. 2003, *Astrophys. J.*, 596, 860
- Mingarelli, C. M. F., Grover, K., Sidery, T., Smith, R. J. E., & Vecchio, A. 2012, *Phys. Rev. Lett.*, 109, 081104
- Misner, C. W., Thorne, K. S., & Wheeler, J. A. 1973, *Gravitation* (San Francisco: W.H. Freeman and Co., 1973)
- Moore, C. J., Taylor, S. R., & Gair, J. R. 2015, *Classical and Quantum Gravity*, 32, 055004
- Peters, P. C. 1964, *Phys. Rev.*, 136, B1224
- Peters, P. C., & Mathews, J. 1963, *Phys. Rev. D*, 131, 435
- Peterson, B. M., et al. 2004, *Astrophys. J.*, 613, 682
- Piero, V., Pinto, I. M., Spallicci, A. D., Laserra, E., & Recano, F. 2001, *MNRAS*, 325, 358
- Piran, T., Nakar, E., & Rosswog, S. 2013, *MNRAS*, 430, 2121
- Rajagopal, M., & Romani, R. W. 1995, *The Astrophys. J.*, 446, 543
- Roedig, C., Dotti, M., Sesana, A., Cuadra, J., & Colpi, M. 2011, *MNRAS*, 415, 3033
- Roedig, C., & Sesana, A. 2012, *Journal of Physics Conference Series*, 363, 012035
- Rosado, P. A., Sesana, A., & Gair, J. 2015, ArXiv e-prints
- Sesana, A. 2010, *The Astrophysical Journal*, 719, 851
- Sesana, A. 2013, *Classical and Quantum Gravity*, 30, 224014
- Sesana, A., Gualandris, A., & Dotti, M. 2011, *MNRAS*, 415, L35
- Sesana, A., Haardt, F., & Madau, P. 2008, *Astrophys. J.*, 686, 432
- Sesana, A., & Vecchio, A. 2010, *Classical and Quantum Gravity*, 27, 084016
- Sesana, A., & Vecchio, A. 2010, *Physical Review D*, 81, 104008
- Sesana, A., Vecchio, A., & Volonteri, M. 2009, *MNRAS*, 394, 2255
- Soltan, A. 1982, *MNRAS*, 200, 115
- Tanvir, N. R., Levan, A. J., Fruchter, A. S., Hjorth, J., Hounsell, R. A., Wiersema, K., & Tunnicliffe, R. L. 2013, *Nature*, 500, 547
- Taylor, S., Ellis, J., & Gair, J. 2014, *Phys. Rev. D*, 90, 104028
- Thorne, K. S. 1987, in *Three hundred years of gravitation*, ed. S. Hawking & W. Israel (Cambridge University Press), 330–458
- van Haasteren, R., & Levin, Y. 2013, *MNRAS*, 428, 1147
- Watson, G. 1995, *A Treatise on the Theory of Bessel Functions*, Cambridge Mathematical Library (Cambridge University Press)
- Wyithe, J. S. B., & Loeb, A. 2003, *The Astrophys. J.*, 590, 691
- Yardley, D. R. B., et al. 2010, *MNRAS*, 407, 669
- Yunes, N., Arun, K. G., Berti, E., & Will, C. M. 2009, *Phys. Rev. D*, 80, 084001
- Zhu, X.-J., et al. 2015, *MNRAS*, 449, 1650